ACS central science

http://pubs.acs.org/journal/acscii

Research Article

Quasi-Orthogonal Configuration of Propylene within a Scalable Metal−Organic Framework Enables Its Purification from Quinary Propane Dehydrogenation Byproducts

Peng Hu,[§] Jialang Hu,[§] Hao Liu, Hao Wang, Jie Zhou, Rajamani Krishna,* and Hongbing Ji*

Cite This: *ACS Cent. Sci.* 2022, 8, 1159−1168

Read Online

ACCESS | Metrics & More | Article Recommendations | Supporting Information

ABSTRACT: Propylene production via nonoxidative propane dehydrogenation (PDH) holds great promise in meeting growing global demand for propylene. Effective adsorptive purification of a low concentration of propylene from quinary PDH byproducts comprising methane (CH_4), ethylene (C_2H_4), ethane (C_2H_6), propylene (C_3H_6), and propane (C_3H_8) has been an unsolved academic bottleneck. Herein, we now report an ultramicroporous zinc metal−organic framework (Zn-MOF, termed as **1**) underlying a rigid one-dimensional channel, enabling trace C_3H_6 capture and effective separation from quinary PDH byproducts. Adsorption isotherms of **1** suggest a record-high C_3H_6 uptake of 34.0/92.4 cm^3 cm^{-3} (0.01/0.1 bar) at 298 K. In situ spectroscopies, crystallographic experiments, and modeling have jointly elucidated that the outstanding propylene uptakes at lower pressure are dominated by multiple binding interactions and swift diffusion behavior, yielding quasi-orthogonal configuration of propylene in adaptive channels. Breakthrough tests demonstrate that 30.8 L of propylene with a serviceable purity of 95.0−99.4% can be accomplished from equimolar C_3H_6/C_3H_8 mixtures for 1 kg of activated **1**. Such an excellent property is also validated by the breakthrough tests of quinary mixtures containing $CH_4/C_2H_4/C_2H_6/C_3H_6/C_3H_8$ (3/5/6/42/44, v/v/v/v/v). Particularly, structurally stable **1** can be easily synthesized on the kilogram scale using cheap materials (only $167 for per kilogram of **1**), which is important in industrial applications.

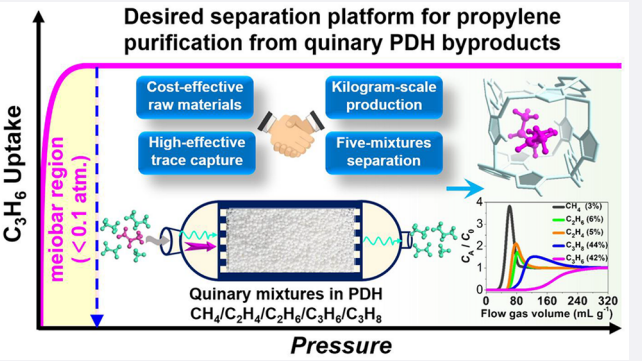

1. INTRODUCTION

Propylene (C_3H_6), as one of the most important chemical products, is widely used in the production of various chemicals, including polymers (e.g., polypropylene) and oxygenates (e.g., acetone and propylene oxide) etc.,[1,2] and is expected to grow above 130 million metric tons by 2023.[3] In the petrochemical industry, nonoxidative propane dehydrogenation (PDH) is becoming popular and is regarded as a promising way to meet the ever-increasing demand for propylene across the globe.[4] The resultant byproducts in PDH reactions including methane (CH_4), ethane (C_2H_6), ethylene (C_2H_4), and propane (C_3H_8) impurities doubtlessly reduce the purity and productivity of C_3H_6. Effective C_3H_6 separation from binary C_3H_6/C_3H_8 mixtures (only 0.04 nm in kinetic diameter, Table S1) and even quinary mixtures in PDH byproducts (typically consisting of ca. 1−3% CH_4, 0.5−6% C_2H_6, 0.2−5% C_2H_4, 40−45% C_3H_8, and 42−50% C_3H_6) is a prerequisite for improving the quality of propylene. The separation technologies currently used are based on energy- and capital-intensive distillation operation, certainly contributing to larger energy loss and economic costs. Adsorbent-based separation strategies could theoretically alleviate the above-mentioned energy consumption without a phase change, namely, distinguishing the gas molecules only through molecule size, shape, polarity, and other characteristics.[5]

Metal−organic frameworks (MOFs), as well-known porous adsorbents, have been extensively explored for gas separation due to their adjustable pore chemistry and structural diversity etc.[6−9] In terms of separation mechanisms, it can be roughly divided into thermodynamic separation and nonequilibrium separation. Compared with unilateral thermodynamic equilibrium dominated by binding affinities, the strategies that rely on nonequilibrium separation (including sieving separation and kinetic-driven separation) can be more energy-efficient and realistic given the fact that industrial pressure swing adsorption (PSA), vacuum swing adsorption (VSA), and temperature swing adsorption (TSA) processes are actually operating under nonequilibrium operating conditions. For example, Chen et al.[10] covered the Co-gallate for sieving

Received: May 9, 2022
Published: July 22, 2022

Scheme 1. Schematic Illustration of Propylene Purification from Propane Dehydrogenation (PDH) Byproducts, Including (a) Obtained Academic Achievements for Binary C_3H_6/C_3H_8 Mixtures and (b) Crucial but Neglected Challenges for C_3H_6 Purification from PDH Byproducts Containing Quinary $CH_4/C_2H_4/C_2H_6/C_3H_6/C_3H_8$ Mixtures

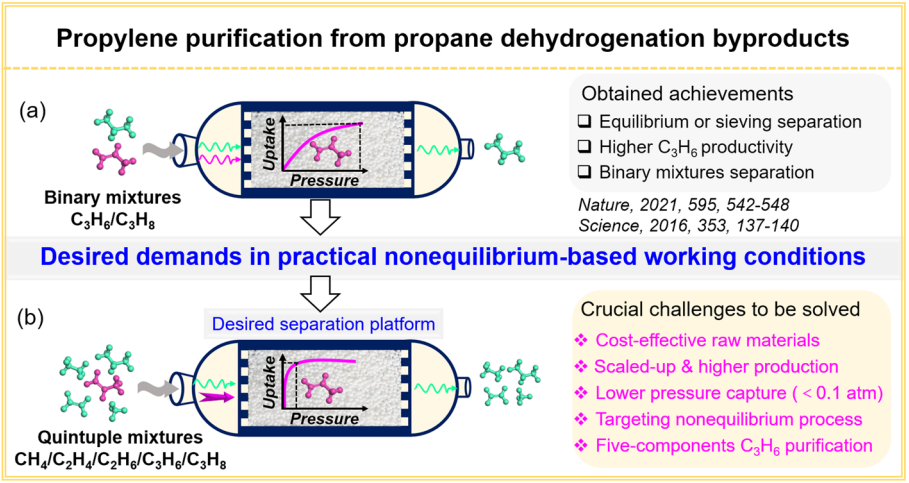

separation of C_3H_6/C_3H_8, which suggested a notable adsorption capacity of 66.6 cm^3 cm^{-3} at 1 bar and 298 K. Breakthrough tests revealed the high purity of propylene (97.7%) with a high dynamic separation productivity of 36.4 cm^3 cm^{-3} under ambient conditions. Another praiseworthy sieving stage, JNU-3a, designed by Li et al.,[11] featured one-dimensional channels with embedded molecular pockets and realized the sieving separation of binary C_3H_6/C_3H_8, yielding high-purity C_3H_6 (≥99.5%) and a C_3H_6 productivity of 53.5 L kg^{-1}. Unfortunately, strong sieving restriction in the pore channels might cause some unavoidable issues associated with the diffusion behavior and regeneration process. From the perspective of structural flexibility, most linkers are flexible in nature; accurately controlling pore size within a critical range to fully sieve C_3H_6 from C_3H_6/C_3H_8 mixtures is still in its infancy. Conversely, the kinetic effects, a significative diffusion-driven mechanism in the nonequilibrium process, could be dexterously designed to effectively accomplish the non-equilibrium separation. Li et al.[12] prepared a MOF (termed as ELM-12), showing an enhanced C_3H_6 uptake of 62.0 mg g^{-1} at 298 K and 1 bar and higher kinetic C_3H_6/C_3H_8 selectivity (204 at 298 K and 971 at 308 K). Breakthrough tests also confirmed the separation performance for binary mixtures, yielding a C_3H_6 productivity of 457 mmol per liter. Also, the Li and Eddaoudi groups developed several MOFs having good kinetic selectivity that could be used for binary C_3H_6/C_3H_8 separation.[13,14] Of particular note is that, albeit conspicuous achievements have been achieved for kinetic separation of C_3H_6/C_3H_8, regrettably, these studies have only focused on binary mixtures. Synergistic kinetic-driven separation of C_3H_6 from quinary mixtures, especially from PDH byproducts containing CH_4, C_2H_6, C_2H_4, and C_3H_8 impurities, has not been realized yet. Another crucial but easily overlooked fact is that the partial pressure of propylene is usually low (<300 mbar) in quinary mixtures,[15] which undoubtedly poses a serious challenge for trace C_3H_6 capture and C_3H_6 purification at a low partial pressure (Scheme 1).

Given the concerns mentioned above, we now report the first paradigm of using an ultramicroporous zinc metal–organic framework (Zn-MOF, termed as **1**) with rigid one-dimensional channels and decent pore chemistry for trace C_3H_6 capture and its purification from quinary PDH byproducts containing CH_4, C_2H_6, C_2H_4, C_3H_6, and C_3H_8 mixtures. Static adsorption isotherms suggest that **1** possesses the record-high C_3H_6 uptake of 92.4 cm^3 cm^{-3} at 298 K and 0.1 atm, indicating a great potential for C_3H_6 capture at lower partial pressure. Further, comprehensive analysis including in situ spectroscopies, crystallographic experiments, and modeling analysis have cooperatively demonstrated that the decent pore microenvironment and multiple task-specific groups enabled synergetic equilibrium effects and "sweet spots" of kinetics for trapping C_3H_6, evidently boosting C_3H_6 separation. In particular, two C_3H_6 molecules adsorbed in one unit cell exhibit an unusual quasi-orthorhombic configuration, which favors the intramolecular interaction and multiple binding models with pore pockets. Breakthrough tests demonstrate that **1** is capable of separating high-purity C_3H_6 (95.0−99.4%) from an equimolar C_3H_6/C_3H_8 mixture under ambient conditions, giving a maximum C_3H_6 productivity of 30.8 L for 1 kg of activated **1** under ambient conditions. The excellent separation property of C_3H_6 on **1** is also validated by the experimental and simulated breakthrough tests of quinary PDH byproducts containing $CH_4/C_2H_4/C_2H_6/C_3H_6/C_3H_8$ (3/5/6/42/44, v/v/v/v/v) mixtures, suggesting that **1** could inherit the preferable separation performance for trapping C_3H_6 from PDH byproducts. Notably, **1** possesses good structural stability and can be easily synthesized on the kilogram scale using cheap raw materials (only $167 for per kilogram of **1**), awarding **1** the potential benchmark stage to purify C_3H_6 from multiple components.

2. EXPERIMENTAL SECTION

2.1. Materials. All reagents and solvents were purchased commercially and used without further processing. Zinc oxalate and 1,2,4-triazole were purchased from Macklin, Shanghai, China. Ethanol (C_2H_5OH, 99.5%) and methanol (CH_3OH, 99.5%) were purchased from Aladdin Industrial Co., Ltd., Shanghai, China.

2.2. Scalable Synthesis of Robust Zn-MOF (1). **1** was prepared according to the following method with some modifications.[16] In detail, zinc oxalate and 1,2,4-triazole were mixed at the molar ratio of 1:2.3, then added into aqueous solution containing methanol/ethanol and ultrasonic stirring.

https://doi.org/10.1021/acscentsci.2c00554
ACS Cent. Sci. 2022, 8, 1159−1168

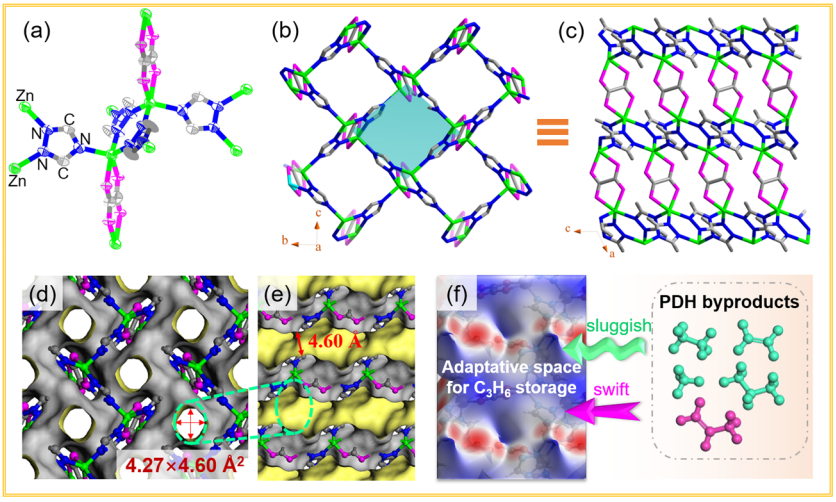

Figure 1. (a) ORTEP plot of the single-crystal X-ray structure of the **1** model with probability ellipsoids drawn at 80%. (b) 3D crystal structure of **1** along the *a* axis. (c) View orthogonal to b showing the pillaring of the zinc triazolate layers by oxalate anions (the different nets are highlighted in bule, pink, bright blue, and gray-40% for clarity (code mode: C in ligands, gray-40%; Zn, bright blue; O, pink). (d) Accessible Connolly surface representation of one-dimensional pore geometry along the *a* axis, with an aperture size of 4.27 × 4.60 Å^2 (excluding van der Waals radii). (e) Diagram of diffusion channels for various guests and (f) the Hirshfeld surface (de) displaying the favorable electrostatic potential for C_3H_6 capture from PDH byproducts containing CH_4, C_2H_6, C_2H_4, C_3H_6, and C_3H_8 mixtures, of which C_3H_6 was drawn in pink and other guests were drawn in green for clarity.

Subsequently, the solutions were transferred to a Teflon autoclave and heated at 453 K for 72 h. The yielded products were then washed with methanol and ethanol and then heated in a vacuum oven at 373 K for 12 h to afford desolvated **1**.

2.3. Dynamic Column Breakthrough Experiments. Dynamic breakthrough experiments were tested in a home-made breakthrough setup and monitored on a gas chromatograph (GC). Prior to the breakthrough experiments, 0.3 g of activated **1** adsorbent was filled into the customized adsorption column (7.0 mm I.D. and 250 mm in length); glass wool was used to plug the two ends of the column. Then, the column was in situ heated at a temperature of 373 K for 12 h with a helium flow (5 sccm) to remove the adsorbed gas impurities. After the system was stabilized, the device was cooled to 298 K, and the gas mixtures of C_3H_6/C_3H_8/He (30/30/40, v/v/v) were introduced into the pipeline. The gas mixtures were passed through the column at a flow rate of 2 sccm and detected through GC. In the regeneration procedure, the adsorbent was in situ heated at 373 K for 12 h through using sweeping He gas at a rate of 5 sccm. For quinary $CH_4/C_2H_4/C_2H_6/C_3H_6/C_3H_8$ (3/5/6/42/44, v/v/v/v/v), 0.01 kg of **1** was filled into the customized adsorption column (21.0 mm I.D. and 250 mm in length; note that the adsorbents were extruded, ground, and sieved into 40−60 mesh particles to minimize the impacts of diffusion and pressure drop). Other procedures were kept the same.

The captured capacity of gas on **1** could be estimated using eq 1:

$$Q = \frac{C_i V}{22.4 \times m} \times \int_0^t \left(1 - \frac{F}{F_0}\right) \mathrm{d}t \qquad (1)$$

where Q is the equilibrium adsorption capacity of gas i (mmol g^{-1}), C_i is the feed gas concentration, V is the volumetric feed flow rate (sccm), t is the adsorption time (min), F_0 and F are the inlet and outlet gas molar flow rates, respectively, and m is the mass of the adsorbent (g).

3. RESULTS AND DISCUSSION

3.1. Structural Analysis of Robust 1. In the case of single unit structure, the Zn center was five-coordinated with a distorted trigonal bipyramidal geometry (Figure 1a). In detail, the nitrogen atoms located in the 1,2-positions of the triazolate coordinated with Zn dimers and further connected to the next dimer via the nitrogen atom in the 4-position of the triazolate, as a result, forming into two-dimensional (2D) lattice planes. Interestingly, the layers of 1,2,4-triazolate-bridged zinc(II) were further pillared by oxalate species to construct the three-dimensional (3D) lattice and 3D pore geometry (Figure 1b,c; a detailed list of atomic positions for the Zn-MOF model are available in Table S2). The crystalline phase and purity of as-prepared bulk **1** was verified by combing the comparisons of theoretical and experimental PXRD diffractions. As clearly shown in Figure S1, all of the experimentally measured characteristic peaks agreed well with the simulated data and crystallized in the *P*21/*c* space group, indicating the isostructural topological structure of **1**. Further, the cell volumes derived from refinement analysis between experimental **1** and the theoretical model gave a $\Delta V/V$ of 0.005% (Table S3), being much lower than that of reported rigid MOF-5 (0.8%).[17] The quais-unchanged cell volume shrinkage revealed the excellent skeleton rigidity of **1**, although indirectly. In order to confirm the structural rigidity under variable-temperature conditions, we conducted PXRD tests at 298 and 373 K to investigate the evolution of the unit cell. As shown in Figure S2a,b, it is suggested that there are no apparent shifts in the positions of all peaks for **1**, revealing a higher framework lattice rigidity and structure stability without phase changes observed. In addition, the cell volumes of **1** at 298 (Figure S2a) and 373 K (Figure S2b) afforded a $\Delta V/V$ of 0.02% (Table S3). Intuitively, the cell structures of **1** underwent quasi-unchanged conformation deformations (Figure S2c,d) compared with that of theoretical topology, suggesting a credible structure stability. The excellent structure stability was

https://doi.org/10.1021/acscentsci.2c00554
ACS Cent. Sci. 2022, 8, 1159−1168

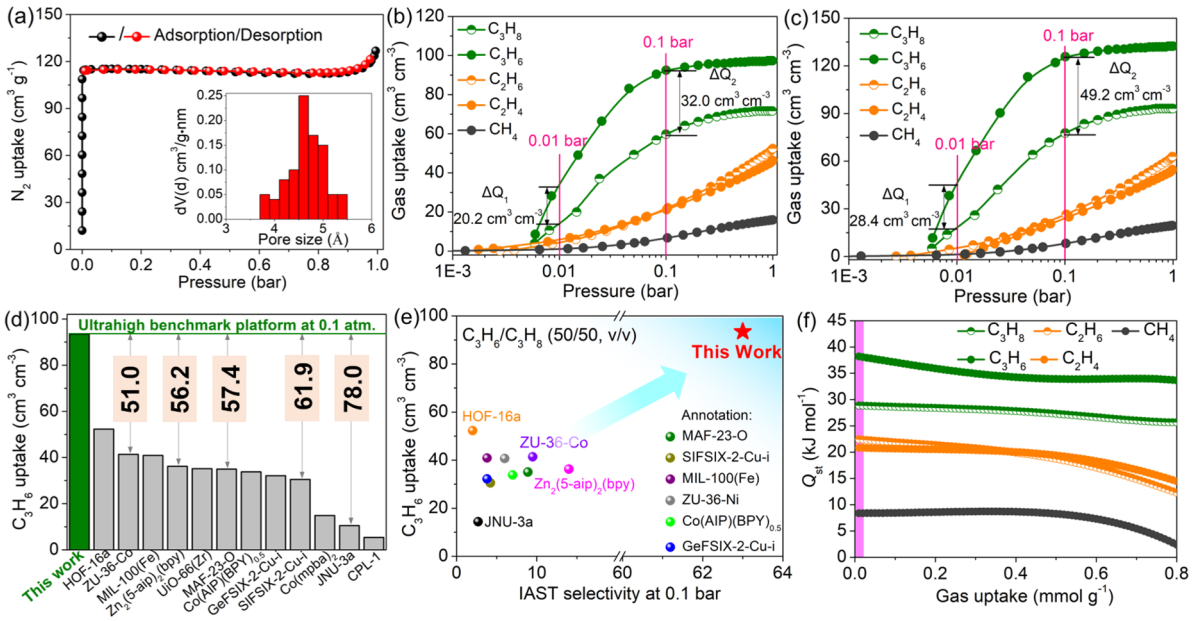

Figure 2. (a) N_2 adsorption isotherms at 77 K and 1 bar. (b,c) Single-gas adsorption isotherms of various molecules at (b) 298 K and (c) 273 K, respectively, with a pressure of 1 bar. (d) Comparisons of volumetric uptake of C_3H_6 on **1** and well-known adsorbents at 298 K and 0.1 bar. (e) Comparisons of IAST selectivity of C_3H_6/C_3H_8 (50/50, v/v) versus C_3H_6 uptake on **1** and benchmark materials at 298 K and 0.1 bar. (f) Coverage-dependent adsorption enthalpy profiles of various guest molecules on **1** obtained by the virial fitting method.

also demonstrated by TGA analysis (Figure S3), yielding a higher decomposition temperature exceeding 600 K.

Intuitional visualization of pore conformation, the simulated Connolly pore surface exhibited a zigzag shaped one-dimensional pore geometry along the crystallographic *a* axis, with a cross-sectional size of ca. 4.27 × 4.60 Å^2 (Figure 1d,e; excluding the distances of the van der Waals radii), which would be favorable for distinguishing the gas diffusion behaviors. Especially for C_3H_6 and C_3H_8 guests with highly similar molecular attributes, the decent pore window seemed to be unfulfillable for both C_3H_8 (with the kinetic diameter of 5.1 Å) and C_3H_6 (4.7 Å) to diffusion into the pore channels from the kinetic diameter point of view. Nevertheless, the suitable pore space and the van der Waals molecular dimension differentiation could be expected to realize the separation of C_3H_8 (4.20 × 4.80 × 6.80 Å^3) and C_3H_6 (4.16 × 4.65 × 6.45 Å^3; Table S1). Thus, the propylene molecule with a minimum cross-section size of 4.16 × 4.65 Å^2 or 19.34 Å^2 could theoretically diffuse into the channel of **1** with a contented cross-section size (4.27 × 4.60 Å^2 or 19.64 Å^2), while propane with a minimum cross-section size of 4.20 × 4.80 Å^2 or 20.16 Å^2 would be excluded from the pore channels due to the limited cross-section size of **1**. Note that this slight shape sieving may not achieve an ideal sieving effect, but it is important to influence the diffusion behavior of molecules. A deep insight into the Hirshfeld surface (Figure 1f) is that it can be observed that a highly attractive negative electrostatic potential mapped with −0.05 au (red) was clearly distributed in the pore channel, suggesting the enriched pore polarity, which favored the binding interaction with the molecule that had a larger dipole moment.[18,19] In brief, due to decent molecule dimensions and the large dipole moment of C_3H_6, it is expected to form strong interactions with the polar pore surface and will effortlessly diffuse into the adaptive pore channel.

3.2. Isothermal Adsorption and Selectivity Analysis.

The eternal pore attributes of **1** were determined at 77 K through using N_2 as the probe molecule. As clearly seen in Figure 2a, **1** exhibited a representative I-type profile, yielding a N_2 capacity of 127.4 cm^3 g^{-1} at 1 atm. The Brunauer−Emmett−Teller (BET) surface area and pore volume were evaluated to be 526.1 m^2 g^{-1} and 0.35 cm^3 g^{-1} by adopting the ASAP 2020 physisorption analyzer, being nearly identical to the theoretical values of 510.8 m^2 g^{-1} and 0.29 cm^3 g^{-1} (calculated from the optimized crystal structure). The pore size distribution (PSD) according to the Horvath−Kawazoe model revealed the ultramicropore with a peak centered at ca. 4.62 Å (inset in Figure 2a). The permanent ultraporosity and the decent pore dimensions motivated us to explore the potential adsorption performance of propane dehydrogenation byproducts including CH_4, C_2H_4, C_2H_6, C_3H_6, and C_3H_8 on activated **1**. We collected the single-component adsorption isotherms of various guests on **1** at 298 K up to 1 atm. Here, volumetric uptake is adopted to evaluate the adsorption performance of the adsorbents in industry as that would determine the footprint of the gas separation units.[20] As clearly depicted in Figure 2b, **1** exhibited a distinguished C_3H_6 adsorption steepness at lower concentrations of 0.01−0.1 bar, giving the ultrahigh volumetric C_3H_6 uptakes of 34.0/92.4 cm^3 cm^{-3} (0.01/0.1 bar) at 298 K, as revealed by the steepness of the C_3H_6 adsorption isotherms. Conversely, it indicated eclipsed adsorption capacity for other guest molecules under identical conditions (Figure 2b). Further increasing pressure to 1 bar, **1** suggested quasi-saturated capacity of 97.4 cm^3 cm^{-3}, corresponding to 9.4 wt % or 1.94 C_3H_6 molecule per cell unit. In addition, the differences of statical adsorption capacity (denoted as ΔQ) for C_3H_6 and C_3H_8 at a lower pressure of 0.01/0.1 bar afforded ΔQ_1 and ΔQ_2 values of 20.2 and 32.0 cm^3 cm^{-3} at 298 K (Figure 2b), confirming the preference for trapping trace C_3H_6 under lower partial pressure. Such differences could be visually observed at 273 K (Figure 2c).

https://doi.org/10.1021/acscentsci.2c00554
ACS Cent. Sci. 2022, 8, 1159−1168

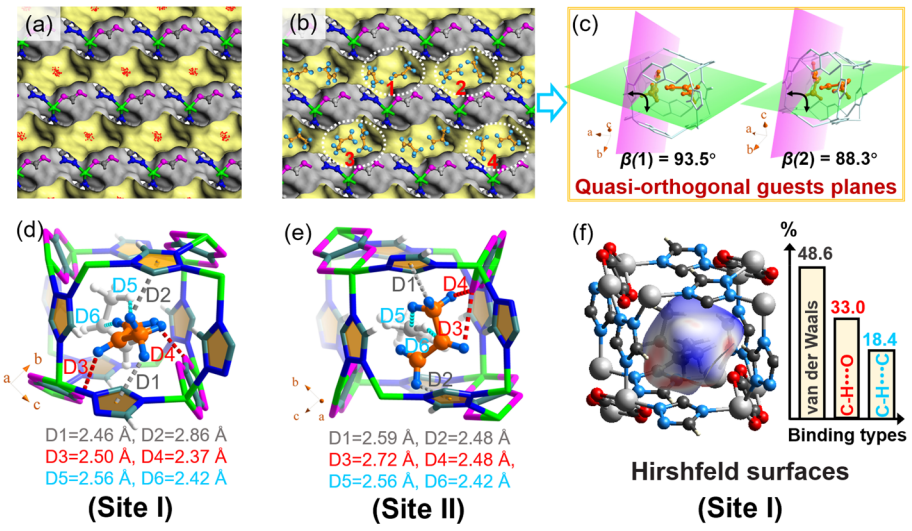

Figure 3. (a) Density distribution of C_3H_6 molecules within **1** topology obtained from GCMC simulations. (b) Side views of the packing diagram of the C_3H_6 adsorbed in the framework of **1**. (c) Visualized planes of guest molecule yielded from b (**1** and **2**, marked with red color) and created by three C atoms on a molecule (the atoms in guest molecules are highlighted with orange and other atoms in MOF structure are highlighted with light turquoise for clarity). (d) DFT calculated adsorption conformation of C_3H_6-loaded **1** in site I and (e) DFT calculated adsorption conformation of C_3H_6-loaded **1** in site II (note that the binding types are colored in gray, red, and turquoise, corresponding to van der Waals interaction, hydrogen-bonding, and intramolecular forces; color modes: H in ligands, white; H in guest molecule, light blue; Zn, bright green; O, pink; N, blue; C, sea green). (f) Hirshfeld surface (de) displaying host−guest interactions of C_3H_6-loaded **1** in site I.

Apparently, **1** revealed the enhanced C_3H_6 uptake, with values of 45.3/125.4/133.4 cm^3 cm^{-3} (0.01/0.1/1 bar), and the ΔQ values between C_3H_6 and C_3H_8 were up to 28.4/49.2/40.0 cm^3 cm^{-3} for 0.01/0.1/1 bar, respectively. In addition, according to the saturated C_3H_6 capacity, the density of gaseous C_3H_6 in **1** was determined to be 281.3 g L^{-1} at 298 K and 0.1 bar. To our knowledge, the storage density of confined C_3H_6 in the channel far surpassed that of other benchmark materials including $Zn_2(5\text{-aip})_2(bpy)$ (135.9 g L^{-1}),[20] SIFSIX-2-Cu-i (135.5 g L^{-1}),[22] and CPL-1 (43.7 g L^{-1})[23] etc. Such a higher storage density of C_3H_6 at 0.1 atm was more than 164-fold higher than that of gaseous C_3H_6 (1.707 g L^{-1}) under similar conditions, suggesting that cooperative stacking models or intramolecular binding affinities may be responsible for C_3H_6 capture under lower pressure. Such an unusual adsorption configuration for trace C_3H_6 capture on **1** was mainly attributed to the larger polarizability/dipole moment of C_3H_6 (Table S1), which exerted a crucial effect on the purification of propylene at lower concentrations, especially for propane cracking-gas mixtures containing multiple components.

In order to further highlight the advantages of **1** at low pressure, detailed comparisons with other advanced materials were integrated at 298 K and 0.1 bar. Results evidenced that **1** remained the record-high volumetric capacity of C_3H_6 (92.4 cm^3 cm^{-3}), surpassing that of most state-of-the-art competitors, including the newly reported MOF platforms ZU-36-Co (41.4 cm^3 cm^{-3}),[24] $Zn_2(5\text{-aip})_2(bpy)$ (36.2 cm^3 cm^{-3}),[21] and JNU-3a (14.4 cm^3 cm^{-3}),[25] etc. (Figure 2d). To quantitatively evaluate the separation potential of **1** for binary C_3H_6/C_3H_8 mixtures, the ideal adsorbed solution theory (IAST) selectivity was evaluated using the double site Langmuir−Freundlich (DSLF) model (Figure S4a,b and Table S5).[26,27] Obviously, **1** indicated a remarkable C_3H_6/C_3H_8 IAST selectivity, with a value of 63 at 0.1 bar (Table S4), far ascendant to many C_3H_6-selective prototypes covered, including MAF-23-O (8.9),[28] $Zn_2(5\text{-aip})_2(bpy)$ (14.2),[21] and MIL-100(Fe) (3.8).[29] In addition, the comprehensive comparisons between C_3H_6 uptakes and the selectivity of C_3H_6/C_3H_8 at 0.1 bar suggested that **1** ranked in the "ceiling" level (Figure 2e), uncovering that **1** can effectively overcome the obstacles in balancing insurmountable "trade-off" effects. The unwonted breakthrough in trapping trace C_3H_6 is of the utmost importance, especially from multiple components with lower partial pressures of propylene. Note that IAST methods are often subject to uncertainties and limited requirements, and large errors can arise from narrow pores (nonideal gas solution), framework flexibility, a large binding difference, etc. So, the IAST selectivites were calculated here just for qualitative comparison.[30] The coverage-dependent isosteric adsorption heats (Q_{st}) were calculated using the virial method (Figure 2f and Table S6) to explore the interaction energies between various molecules and the host framework. Apparently, the Q_{st} of **1** at zero coverage followed the hierarchy of C_3H_6 (38.3 kJ mol^{-1}) > C_3H_8 (28.9 kJ mol^{-1}) > C_2H_6 (22.4 kJ mol^{-1}) > C_2H_4 (20.7 kJ mol^{-1}) > CH_4 (8.2 kJ mol^{-1}; Figure 2f), conferring **1** with the obvious potential stage to capture C_3H_6 from propane dehydrogenation byproducts. To be noted, the Q_{st} of C_3H_6 at zero coverage was much lower than that of known $Zn_2(5\text{-aip})_2(bpy)$ (46 kJ mol^{-1})[21] and MAF-23-O (54 kJ mol^{-1}),[28] being comparable to SIFSIX-2-Cu-I (35.8 kJ mol^{-1})[22] and ZU-36-Co (38.0 kJ mol^{-1}).[31] The desorption activation energy of C_3H_6 obtained from the TPD profiles was calculated to be 41.5 kJ mol^{-1} (Figure S5a,b), also evidently confirming the strong binding affinity between C_3H_6 and the framework. Such a low adsorption enthalpy not only awarded the **1** platform a lower regeneration energy to yield higher C_3H_6 productivity but also avoided C_3H_6 oligomerization/polymerization that may damage the binding sites.

3.3. Adsorption Conformation and Binding Mechanism. To deeply elucidate the binding sites, we adopted Grand Canonical Monte Carlo (GCMC) simulations to investigate the binding models and adsorption mechanism between guest molecules and **1**. As obviously observed, the simulated adsorption isotherms on **1** agreed well with the experimental

https://doi.org/10.1021/acscentsci.2c00554
ACS Cent. Sci. 2022, 8, 1159−1168

results on the overall trend at 298 K, although some points at ultralow pressure and higher pressure were not particularly intimate (Figure S6). The inconsistent paces may derive from the strong binding affinity between guest molecules and the framework, which were intractable to construct the topology models using simple force fields. Additionally, the visualized density distribution contours of C_3H_6-loaded **1** (Figure 3a) suggested that the adsorbed C_3H_6 was concentrated and arranged in the pore space one by one in a straight line along the zigzag shaped open channels. The optimized C_3H_6 configurations obtained from GCMC-simulated saturated capacity also indicated 2-fold disordering over two binding conformations with partial occupancy, which oriented linearly with its C═C axis along the channels and tilted with its minimum cross-section along the pore wall (Figure 3b). The saturated adsorption orientation in the pore pocket would minimize any possible steric hindrance and electrostatic repulsion from the polar framework. Further, the spatial stacking conformation of two C_3H_6 molecules located at labels **1** and **2** (Figure 3b, highlighted with red color) were amplified and shown in geometrical-plane perspectives (Figure 3c). Note that in order to intuitively mirror the stacking models of the two molecules, the C═C−C bond in a single molecule was selected as the reference point to construct the conformational plane. Interestingly, two C_3H_6 molecules located in one unit cell adopted a quasi-orthogonal arrangement from a static view, giving the dihedral angles of 93.5° for label **1** and 88.3° for label **2** (Figure 3c), respectively. Likewise, for the C_3H_6 molecules located at labels **3** and **4**, the geometrical planes also displayed quasi-orthogonal packing models, with dihedral angles of 96.4° for label **3** and 90.5° for label **4** (Figure S7). Such an orthogonal array of C_3H_6 molecules would maximize its binding interactions with a polar pore surface and favor its preferential capture.

Subsequently, density functional theory (DFT) optimizations of GCMC derived host−guest structures showed that there were mainly two adsorption sites (termed as site I and site II) for C_3H_6-loaded **1** (Figure 3d,e and Table S7), being well located at the unit cell through multiple binding interactions. In detail, for C_3H_6-adsorbed **1** in site I, two hydrogen atoms in the methyl group were grasped through forming chummy van der Waals interactions (C−H···π) with adjacent triazole ligands, giving binding distances of 2.46 Å (D1) and 2.86 Å (D2), respectively (Figure 3d). Meanwhile, another hydrogen atom in the propenyl group and the one in the methyl group were confined through forming additional hydrogen bonds with the oxygen atom in the oxalate ion, yielding shorter distances of 2.50 Å (D3) and 2.37 Å (D4). It should be noted that the latent intramolecular interaction between two C_3H_6 molecules also favored the C_3H_6 adsorption. As visually observed in Figure S8, the static conformation of C_3H_6 adsorbed in site I after geometry optimization oriented linearly with its C═C axis along the vertical direction of the propylene plane in site II for yielding intramolecular affinities through forming Lewis acid/base interactions, yielding a binding distance ($C^{\delta-}\cdots H^{\delta+}$) of 2.56 Å for D5 and 2.42 Å for D6 (Figure 3d and Figure S8). Similar with that in site I, other C_3H_6 molecule in site II were also confined through strong binding affinities. As seen in Figure 3e, in addition to the mentioned intramolecular interaction (namely D5 and D6, inset in Figure 3d), the hydrogen atoms in the methyl group and methylene group were spatially captured with a combination of the van der Waals effects (distance: 2.59 Å for D1 and 2.48 Å for D2). In addition, other H atoms in the propenyl and methyl groups were well immobilized through hydrogen-bond interactions with oxygen atoms (distance: 2.72 Å for D3 and 2.48 Å for D4; Figure 3e). On the contrary, for C_3H_8-loaded **1**, it suggested a weaker binding interaction, although having two adsorption sites (detailed adsorption configurations are available in Figure S9a,b). The theoretical binding energies between the host and guest showed an expected Q_{st} order of C_3H_6 (**1** (38.9 kJ mol^{-1}) > C_3H_8 (**1** (26.4 kJ mol^{-1}), which was consistent with that obtained from experimental results (38.3 kJ mol^{-1} for C_3H_6 and 28.9 kJ mol^{-1} for C_3H_8; Figure 2f). Notably, the binding interactions between the gas molecules and framework were modest (van der Waals interaction, hydrogen bonding, and electrostatic interaction in nature), indicating that enriched C_3H_6 can then be recovered with high purity during the regeneration step.

To further elucidate the unwonted geometrical conformation and adsorption mechanism of C_3H_6 in the **1** skeleton, an in situ PXRD test and Rietveld structural refinements of C_3H_6-loaded **1** were carefully analyzed. As shown in Figure S10a, the refined lattice parameters (a = 8.9427 Å, b = 9.7210 Å, c = 9.5827 Å) of C_3H_6-loaded **1** seemed to be somewhat larger than that of pristine **1** (a = 8.9139 Å, b = 9.6932 Å, c = 9.4836 Å; Table S3), attributed to C_3H_6 occupation in the unit cell of **1**. An intuitional binding scenario (Figure S10b,c) yielded from structural refinements demonstrated that the geometry configurations derived from in situ crystallographic experiments were quasi-consistent with those calculated by theoretical DFT calculations (Figure 3d,e). By comparing the binding distances of the same binding types obtained from experimental and theoretical results, the low relative errors are between 0.0 and 3.1% (Table S8). Such lower relative errors further reveal that the adsorption conformation yielded from crystallographic tests were convincing. In addition, the geometrical planes of two C_3H_6 molecules also exhibited an approximate orthogonal adsorption configuration from a static view, with a dihedral angle of ca. 93.1° (Figure S10d), being consistent with that obtained from theoretical values.

Further, in situ Fourier transform infrared (FT-IR) tests were recorded to reveal the potential host−guest interaction between C_3H_6 and **1**. As clearly shown in Figure S11a, the peaks located in 1630, 1320, and 1171 cm^{-1} in both activated **1** and C_3H_6-loaded **1** were assigned to the C═N adsorption band, symmetric carbonyl stretching, and C−O stretching vibrations in **1** structure.[32−34] While for C_3H_6-loaded **1**, some characteristic peaks associated with the propylene molecule were clearly observed. For example, the emerging peaks located at about 2924 and 1436 cm^{-1} could be attributed to symmetric C−H bending of terminal methyl and methylene motifs in propylene.[35,36] Also, the peak at around 996 cm^{-1} was the C−C stretching mode in propylene.[37] Such spectral changes evidently confirmed the fact that propylene molecules could be adsorbed in the **1** structure. We investigated in situ Raman spectra of C_3H_6-loaded **1** to carefully analyze the host−guest interaction. As explicated in Figure S11b, the peak concentrated at 3147 cm^{-1} was the stretching mode of the C−H bond in the triazole ring of the **1** structure,[38] and the other Raman vibration of the triazole ring (i.e., heterocyclic methyl C−H bending) could be observed at 1477 cm^{-1}.[38] In addition, it was also found that there was an emerging peak that appeared at 1624 cm^{-1}, corresponding to the C═C stretching vibrations in the propylene molecule. This value was downshifted in

https://doi.org/10.1021/acscentsci.2c00554
ACS Cent. Sci. 2022, 8, 1159−1168

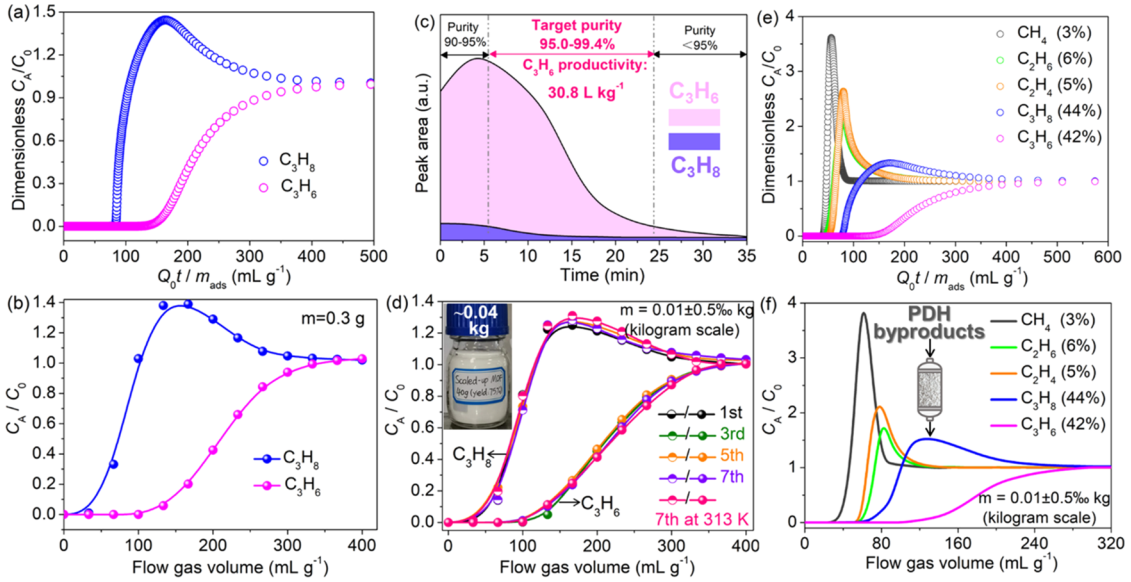

Figure 4. (a) Simulated breakthrough curves of **1** for C_3H_6/C_3H_8/He (30/30/40, v/v/v) at 298 K. (b) Experimental breakthrough curves of **1** for C_3H_6/C_3H_8/He (30/30/40, v/v/v) at 298 K and 1 bar, with a flow rate of 2 sccm. (c) Desorption curves of adsorbed C_3H_6 and C_3H_8 through helium purge, with a flow rate of 5 sccm. (d) Cycling breakthrough experiments of **1** for C_3H_6/C_3H_8/He (30/30/40, v/v/v) over eight cycles (inset represents the scaled-up production on the kilogram level). (e) Simulated breakthrough curves and (f) experimental breakthrough curves of **1** for quinary $CH_4/C_2H_4/C_2H_6/C_3H_6/C_3H_8$ (3/5/6/42/44, v/v/v/v/v) mixtures at 298 K and 1 bar.

comparison with that for gaseous propylene, which was 1640 cm^{-1},[39] mainly ascribed to the formed binding interaction between propylene and the framework, as demonstrated by Yaghi.[40] The negative shift to lower frequency could also be visualized for the Zn−N peak (Figure S11b). Obviously, the Zn−N peak of **1** also experienced a downshift behavior upon propylene adsorption on **1**, suggestive of potential adsorption sites between propylene and **1**.

In addition, Hirshfeld surface analysis was used for probing the host−guest interactions and quantifying the binding interaction types. Hirshfeld surface was a novel partitioning of crystal space, affording a unique 3D d_{norm} surface which could further be resolved into a 2D fingerprint plot.[41] As shown in Figure 3f, it revealed the Hirshfeld surfaces of adsorbed C_3H_6 in site I mapped over d_{norm}, where the larger red spots in the map indicated strong short-range interactions with close contact effects (i.e., hydrogen-bonding) and a negative d_{norm} value. White spots corresponded to contacts around the van der Waals separation and with a d_{norm} value of zero, and blue spots reflected the long-range binding contact with a positive d_{norm} value.[42,43] Clearly, for C_3H_6-loaded **1** at site I, hydrogen-bonding interactions (red spots) and van der Waals effects (white spots) reflected in the map (Figure 3f) were basically consistent with the results obtained by DFT calculations (Figure 3d). Further, the binding types could be quantified by plotting two-dimensional (2D) fingerprint plots. Results showed that van der Waals interaction occupied 48.6% of the total Hirshfeld surface, while hydrogen bonding and intramolecular interaction occupied 33.0 and 18.4%, albeit not being particularly precise. Such consistence also could be found for the C_3H_6 molecule adsorbed at site II (Figure S12).

3.4. Molecular Dynamics and Diffusion Analysis. Diffusion-driven adsorption behavior, a realistic and significative separation metric in industrial PSA, VSA, and TSA-based nonequilibrium working conditions, needed to be given enough attention. We hereby adopted a molecular dynamics (MD) method to probe the diffusion behavior of guest molecules in channels. During the simulations, the initial configurations for the MD simulations were produced by GCMC simulation; the host framework and the gas molecule were both regarded as rigid. As shown in Figure S13 and Table S9, MD-derived diffusion coefficients of $CH_4/C_2H_6/C_2H_4/C_3H_8/C_3H_6$ for **1** were calculated as 0.217/0.717/0.517/13.3/258 × 10^{-11} m^2 s^{-1}. Therefore, the obtained diffusion coefficient of C_3H_6 (258 × 10^{-11} m^2 s^{-1}) on **1** was much higher than that of the covered UiO-66 analogue (97.8 × 10^{-12} m^2 s^{-1})[44] and MAF-23-O (0.82 × 10^{-10} m^2 s^{-1}),[28] confirming the fast diffusion rate. The obtained diffusion selectivity of C_3H_6/C_3H_8 was calculated to be 19.4, which was eclipsed compared with that of MAF-23-O (112.3). Intuitional snapshots of the MD results with both the host and guests as rigid suggested that two C_3H_6 molecules can be adaptively located in the confined channel of **1** after being steadily confined in the pore pocket (Figure S14b), yet that in **1** seemed to be escaping from the host when entering the aperture of the host framework (Figure S14a). Such transient diffusion trajectories further confirmed the favorable diffusion intension for trapping C_3H_6 molecule.

3.5. Dynamic Column Breakthrough Experiments. To further explore separation natures of propylene on **1** from imitated propane dehydrogenation byproducts, transient breakthrough simulations were first probed for C_3H_6/C_3H_8/He (30/30/40, v/v/v) mixtures in a column adsorption−desorption cycle. Simulation results suggested that C_3H_6/C_3H_8 mixtures with distinct breakthrough time could be effectively separated (Figure 4a), yielding a higher C_3H_6 capture capacity of 51.5 L kg^{-1}. These excellent breakthrough results from simulation motivated us to evaluate the separation performance of **1** in the actual separation process. As shown in Figure 4b, C_3H_8 first broke through the adsorption bed, while targeted C_3H_6 was still captured over a flow gas volume of 100 mL g^{-1}. To be noted, the simulated breakthroughs are sharper than those observed experimentally, mainly attributed to the fact that, in the simulations, intracrystalline diffusional influences

https://doi.org/10.1021/acscentsci.2c00554
ACS Cent. Sci. 2022, 8, 1159−1168

are ignored.[26] The captured C_3H_6 and C_3H_8 uptakes were also calculated to be ca. 52.0 and 2.0 L kg^{-1}, giving the outstanding experimental selectivity (or separation factor) of 26. Such a value was much higher than that of other benchmark materials including ZU-36-Ni (19.1),[31] MAF-23-O (15),[28] and Co(AIP)$(BPY)_{0.5}$ (2.92)[45] etc. We also evaluated the captured amount and experimental selectivity with other well-known materials to demonstrate the "trade-off" effects (namely incompatible adsorption capacity and selectivity). As obviously seen in Figure S15, **1** was compatible with adsorption capacity and selectivity, anticipated to be a late-model paradigm for trace C_3H_6 purification.

In addition to the capacity and adsorption selectivity mentioned above, the productivity and purity of C_3H_6 yielded from desorption operation were also two important metrics to assess the separation performance of adsorbents. Apparently, the outlet concentration of the C_3H_6 product was much higher than that of the C_3H_8 competitor, and the whole desorption process can be fully desorbed within 35 min (Figure 4c). The obtained C_3H_6 purities at different time periods were somewhat different, among which the obtained propylene purity between 5.4 and 24.3 min was up to 99.4%, albeit being somewhat overshadowed with actual requirements (≥99.5%) required by the polymer-grade purity of propylene.[46] In addition, it could be estimated that about 30.8 L of the C_3H_6 product with a serviceable purity of 95.0−99.4% could be accomplished from the equimolar C_3H_6/C_3H_8 mixtures for 1 kg of activated **1** in a single breakthrough operation. Such higher productivity and purity far exceeded that of KAUST-7 (16.3 L kg^{-1} with 90.0% purity) and Y-abtc (1.3 L kg^{-1} with 90.0% purity), yet was inferior in comparison to the laudable precedent, i.e., JNU-3a (34.2 L kg^{-1} with 99.5% purity) reported so far.[11] In actual industrial separation units, there is a huge gap between laboratory pilot studies and commercial applications, making mass production of MOFs on a large scale a strong necessity. Here, kilogram scale breakthrough tests were conducted through filling 0.01 ± 0.5‰ kg of activated **1** into the customized column. As revealed in Figure 4d, **1** could still retain the quasi-unchanged separation performance for eight cycles, even in the presence of flow moisture having a certain temperature. The PXRD spectra after eight cycles still kept its intact crystalline structure when immersed in water for 1 week (Figure S16), echoing well with its excellent structural rigidity and stability.

Although **1** suggested efficient C_3H_6 separation from C_3H_6/C_3H_8 binary mixtures, there are tremendous current impediments and challenges in the recovery of valuable propylene from propane dehydrogenation byproducts (typically consisting of ca. 1−3% CH_4, 0.5−6% C_2H_6, 0.2−5% C_2H_4, 40−45% C_3H_8, and 42−50% C_3H_6). Targeting the C_3H_6 purification from quinary mixtures could be expected to earn substantial economic benefits. Transient breakthrough simulations were first predicated with the various feed compositions of $CH_4/C_2H_4/C_2H_6/C_3H_6/C_3H_8$ (3/5/6/42/44, v/v/v/v/v) to assess the universality of **1** for separation of quinary components. As shown in Figure 4e, efficient separation can be accomplished by **1** for quinary mixtures, wherein CH_4, C_2H_6, C_2H_4, and C_3H_8 occurred first, and then C_3H_6 passed through the column after a certain time (τ_{break}). Further, the experimental breakthrough tests were tested in the packed column of **1** under the same gas feed ratios under ambient conditions. The breakthrough profiles described in Figure 4f evidently confirmed that **1** could effectively purify C_3H_6 from imitative propane dehydrogenation byproducts.

3.6. Structural Stability Tests and Costs Evaluation. It is well perceived that structural stability is the first and necessary prerequisite for MOFs to develop from laboratory research to the pilot scale and industry applications. We herein carried out multifaceted investigations on **1**, which had experienced cycling breakthrough experiments, including N_2 adsorption, single-gas adsorption, and crystallographic tests under variable-temperature conditions etc., to systematically analyze the structural stability of **1**. We first probed the pore geometry changes through N_2 adsorption at 77 K. As shown in Figure S17a, the N_2 uptake of **1** still inherited the quasi-unchanged adsorption capacity after cycling breakthrough tests, and the aperture distribution was concentrated at 4.67 Å (inset in Figure S17a), suggesting the unfading ultramicropore nature. In addition, single-gas adsorption isotherms of C_3H_6 on **1** yielded a higher capacity of 31.1−35.0/88.5−94.1 cm^3 cm^{-3} at 0.01/0.1 atm and 298 K after 10 cycles (Figure S17b). Further, the variable-temperature PXRDs of **1** after cycling tests were recorded. As observed in Figure S17c, all of the diffractions all exhibited extremely consistent patterns compared with the theoretical diffractions, indicative of intact structural integrity. The derived top contour plots of variable-temperature PXRD (Figure S17d) evidenced that a main peak shift could hardly be observed, confirming a higher structural rigidity and thermal stability.

Of particular note was that the costs of raw materials should also be taken into account for laboratory-scale synthesis. As visualized in Figure S18 and Table S10, the total costs of raw materials were just $167 for per kilogram of **1** adsorbent, which were much cheaper than other materials, including ZU-36-Ni ($17 399), Fe_2(dobdc) ($4527), and MCF-57 ($10 073) etc. (Table S10), further reinforcing its potential application for C_3H_6 purification. Therefore, the excellent separation performance, steam stability, scalability of production, and cheap costs etc. awarded **1** the prominent potential to purify C_3H_6 from PDH byproducts.

4. CONCLUSIONS

To sum up, an ultramicroporous Zn-MOF with scaled-up production could be easily synthesized using the cost-effective raw materials. An optimized geometry model revealed the ultramicroporous pore conformation for **1**, with a cross-sectional size of 4.27 × 4.60 $Å^2$ (19.64 $Å^2$). The decent pore aperture was slightly larger than that of the propylene molecule with a minimum cross-section size of 4.16 × 4.65 $Å^2$ (19.34 $Å^2$) but less than that of propane molecule with minimum cross-section size of 4.20 × 4.80 $Å^2$ (20.16 $Å^2$), anticipating a diffusion barrier for the highly similar molecules. Static isotherm adsorption suggested that **1** possessed a record-high C_3H_6 uptake of 92.4 cm^3 cm^{-3} at 298 and 0.1 bar, yielding an IAST selectivity of up to 63 among the reported benchmark MOFs. In situ spectroscopies, crystallographic experiments, and modeling demonstrated that two C_3H_6 molecules confined in one unit cell were grasped through multiple binding interaction including van der Waals effects, hydrogen bonding, and intraintermolecular interaction. Molecular dynamics showed that **1** possessed a higher diffusion selectivity of 19.4 for C_3H_6/C_3H_8. Column breakthrough tests demonstrated that about 30.8 L of C_3H_6 product with a purity of 95.0−99.4% could be accomplished from the equimolar C_3H_6/C_3H_8 mixtures for 1 kg of activated **1** in a single breakthrough

https://doi.org/10.1021/acscentsci.2c00554
ACS Cent. Sci. 2022, 8, 1159−1168

operation. Such an excellent separation property of propylene on **1** is also validated by the experimental and simulated breakthrough tests of quinary PDH byproducts containing $CH_4/C_2H_4/C_2H_6/C_3H_6/C_3H_8$ (3/5/6/42/44, v/v/v/v/v). Particularly, structurally stable **1** can be easily synthesized on the kilogram scale using cheap raw materials (only $167 for per kilogram of **1**). The excellent separation performance, steam stability, scalability of production, and cheap costs etc. awarded **1** the prominent potential to purify C_3H_6 from PDH byproducts.

■ ASSOCIATED CONTENT

Supporting Information

The Supporting Information is available free of charge at https://pubs.acs.org/doi/10.1021/acscentsci.2c00554.

Structural characterizations, spectroscopy tests, modeling details, calculation of separation potential, transient breakthrough simulations, supporting figures and tables (PDF)

■ AUTHOR INFORMATION

Corresponding Authors

Hongbing Ji − *Fine Chemical Industry Research Institute, School of Chemistry, Sun Yat-Sen University, Guangzhou 510275, People's Republic of China;* orcid.org/0000-0003-1684-9925; Email: jihb@mail.sysu.edu.cn

Rajamani Krishna − *Van't Hoff Institute for Molecular Sciences, University of Amsterdam, 1098 XH Amsterdam, The Netherlands;* orcid.org/0000-0002-4784-8530; Email: r.krishna@contact.uva.nl

Authors

Peng Hu − *Fine Chemical Industry Research Institute, School of Chemistry, Sun Yat-Sen University, Guangzhou 510275, People's Republic of China*

Jialang Hu − *Fine Chemical Industry Research Institute, School of Chemistry, Sun Yat-Sen University, Guangzhou 510275, People's Republic of China*

Hao Liu − *Fine Chemical Industry Research Institute, School of Chemistry, Sun Yat-Sen University, Guangzhou 510275, People's Republic of China*

Hao Wang − *Fine Chemical Industry Research Institute, School of Chemistry, Sun Yat-Sen University, Guangzhou 510275, People's Republic of China*

Jie Zhou − *Fine Chemical Industry Research Institute, School of Chemistry, Sun Yat-Sen University, Guangzhou 510275, People's Republic of China*

Complete contact information is available at: https://pubs.acs.org/10.1021/acscentsci.2c00554

Author Contributions

[§]These authors contributed equally to this work.

Notes

The authors declare no competing financial interest.

■ ACKNOWLEDGMENTS

This work was financially supported by the National Key Research and Development Program Nanotechnology Specific Project (No. 2020YFA0210900), the National Natural Science Foundation of China (No. 21938001, 21961160741), Guangdong Provincial Key R&D Program (2019B110206002), and the Local Innovative and Research Teams Project of Guangdong Pearl River Talents Program (2017BT01C102). P.H. is also grateful to the China Scholarship Council (CSC) for the financial support (202106380115).

■ REFERENCES

(1) Gao, J.; Cai, Y.; Qian, X.; Liu, P.; Wu, H.; Zhou, W.; Liu, D. X.; Li, L.; Lin, R. B.; Chen, B. A Microporous Hydrogen-Bonded Organic Framework for the Efficient Capture and Purification of Propylene. *Angew. Chem., Int. Ed. Engl.* **2021**, *60*, 20400−20406.

(2) Kong, N.; Fan, X.; Liu, F.; Wang, L.; Lin, H.; Li, Y.; Lee, S. T. Single Vanadium Atoms Anchored on Graphitic Carbon Nitride as a High-Performance Catalyst for Non-oxidative Propane Dehydrogenation. *ACS Nano* **2020**, *14*, 5772−5779.

(3) Hong, A. N.; Yang, H.; Li, T.; Wang, Y.; Wang, Y.; Jia, X.; Zhou, A.; Kusumoputro, E.; Li, J.; Bu, X.; Feng, P. Pore-Space Partition and Optimization for Propane-Selective High-Performance Propane/Propylene Separation. *ACS Appl. Mater. Interfaces* **2021**, *13*, 52160.

(4) Sun, Q.; Wang, N.; Fan, Q.; Zeng, L.; Mayoral, A.; Miao, S.; Yang, R.; Jiang, Z.; Zhou, W.; Zhang, J.; et al. Subnanometer Bimetallic Platinum-Zinc Clusters in Zeolites for Propane Dehydrogenation. *Angew. Chem., Int. Ed. Engl.* **2020**, *59*, 19450−19459.

(5) Wang, Y.; Huang, N. Y.; Zhang, X. W.; He, H.; Huang, R. K.; Ye, Z. M.; Li, Y.; Zhou, D. D.; Liao, P. Q.; Chen, X. M.; et al. Selective Aerobic Oxidation of a Metal-Organic Framework Boosts Thermodynamic and Kinetic Propylene/Propane Selectivity. *Angew. Chem., Int. Ed. Engl.* **2019**, *58*, 7692−7696.

(6) Hu, P.; Hu, J.; Wang, H.; Liu, H.; Zhou, J.; Liu, Y.; Wang, Y.; Ji, H. One-Step Ethylene Purification by an Ethane-Screening Metal-Organic Framework. *ACS Appl. Mater. Interfaces* **2022**, *14*, 15195−15204.

(7) Hu, P.; Liang, X.; Yaseen, M.; Sun, X.; Tong, Z.; Zhao, Z.; Zhao, Z. Preparation of highly-hydrophobic novel N-coordinated UiO-66(Zr) with dopamine via fast mechano-chemical method for (CHO-/Cl-)-VOCs competitive adsorption in humid environment. *Chem. Eng. J.* **2018**, *332*, 608−618.

(8) Hu, P.; Wang, R.; Gao, Z.; Jiang, S.; Zhao, Z.; Ji, H.; Zhao, Z. Improved interface compatibility of hollow H-$Zr_{0.1}Ti_{0.9}O_2$ with UiO-66-NH_2 via Zr-Ti bidirectional penetration to boost visible photocatalytic activity for acetaldehyde degradation under high humidity. *Appl. Catal. B-Environ* **2021**, *296*, 120371.

(9) Hu, P.; Zhao, Z.; Sun, X.; Muhammad, Y.; Li, J.; Chen, S.; Pang, C.; Liao, T.; Zhao, Z. Construction of crystal defect sites in N-coordinated UiO-66 via mechanochemical in-situ N-doping strategy for highly selective adsorption of cationic dyes. *Chem. Eng. J.* **2019**, *356*, 329−340.

(10) Liang, B.; Zhang, X.; Xie, Y.; Lin, R. B.; Krishna, R.; Cui, H.; Li, Z.; Shi, Y.; Wu, H.; Zhou, W.; et al. An Ultramicroporous Metal-Organic Framework for High Sieving Separation of Propylene from Propane. *J. Am. Chem. Soc.* **2020**, *142*, 17795−17801.

(11) Zeng, H.; Xie, M.; Wang, T.; Wei, R. J.; Xie, X. J.; Zhao, Y.; Lu, W.; Li, D. Orthogonal-array dynamic molecular sieving of propylene/propane mixtures. *Nature* **2021**, *595*, 542−548.

(12) Li, L.; Lin, R.; Wang, X.; Zhou, W.; Jia, L.; Li, J.; Chen, B. Kinetic separation of propylene over propane in a microporous metal-organic framework. *Chem. Eng. J.* **2018**, *354*, 977−982.

(13) Peng, J.; Wang, H.; Olson, D. H.; Li, Z.; Li, J. Efficient kinetic separation of propene and propane using two microporous metal organic frameworks. *Chem. Commun. (Camb)* **2017**, *53*, 9332−9335.

(14) Xue, D.-X.; Cadiau, A.; Weselinski, Łu. J.; Jiang, H.; Bhatt, P. M.; Shkurenko, A.; Wojtas, L.; Zhijie, C.; Belmabkhout, Y.; Adil, K.; Eddaoudi, M.; et al. Topology meets MOF chemistry for pore-aperture fine tuning: ftw-MOF platform for energy-efficient separations via adsorption kinetics or molecular sieving. *Chem. Commun. (Camb)* **2018**, *54*, 6404−6407.

(15) Jun, J. W.; Kim, T. W.; Choi, W. C.; Kim, C. U. Propane to light olefins by one-pot cascade and series reactions. *Chem. Eng. J.* **2018**, *377*, 120114.

(16) Al-Attas, T. A.; Marei, N. N.; Yong, X.; Yasri, N. G.; Thangadurai, V.; Shimizu, G.; Siahrostami, S.; Kibria, M. G. Ligand-Engineered Metal-Organic Frameworks for Electrochemical Reduction of Carbon Dioxide to Carbon Monoxide. *ACS Catal.* **2021**, *11*, 7350−7357.
(17) Rowsell, J. L.; Spencer, E. C.; Eckert, J.; Howard, J. A.; Yaghi, O. M. Gas adsorption sites in a large-pore metal-organic framework. *Science* **2005**, *309*, 1350−1354.
(18) Barnett, B. R.; Parker, S. T.; Paley, M. V.; Gonzalez, M. I.; Biggins, N.; Oktawiec, J.; Long, J. R. Thermodynamic Separation of 1-Butene from 2-Butene in Metal-Organic Frameworks with Open Metal Sites. *J. Am. Chem. Soc.* **2019**, *141*, 18325−18333.
(19) Vervoorts, P.; Schneemann, A.; Hante, I.; Pirillo, J.; Hijikata, Y.; Toyao, T.; Kon, K.; Shimizu, K. I.; Nakamura, T.; Noro, S. I.; et al. Coordinated Water as New Binding Sites for the Separation of Light Hydrocarbons in Metal-Organic Frameworks with Open Metal Sites. *ACS Appl. Mater. Interfaces* **2020**, *12*, 9448−9456.
(20) Zhang, Z.; Peh, S. B.; Wang, Y.; Kang, C.; Fan, W.; Zhao, D. Efficient Trapping of Trace Acetylene from Ethylene in an Ultramicroporous Metal-Organic Framework: Synergistic Effect of High-Density Open Metal and Electronegative Sites. *Angew. Chem. Int. Edit* **2020**, *59*, 18927−18932.
(21) Chen, Y.; Wu, H.; Lv, D.; Yuan, N.; Xia, Q.; Li, Z. A pillar-layer metal-organic framework for efficient adsorption separation of propylene over propane. *Sep. Purif. Technol.* **2018**, *204*, 75−80.
(22) Wang, X.; Zhang, P.; Zhang, Z.; Yang, L.; Ding, Q.; Cui, X.; Wang, J.; Xing, H. Efficient Separation of Propene and Propane Using Anion-Pillared Metal-Organic Frameworks. *Ind. Eng. Chem. Res.* **2020**, *59*, 3531−3537.
(23) Chen, Y.; Qiao, Z.; Lv, D.; Duan, C.; Sun, X.; Wu, H.; Shi, R.; Xia, Q.; Li, Z. Efficient adsorptive separation of C_3H_6 over C_3H_8 on flexible and thermoresponsive CPL-1. *Chem. Eng. J.* **2017**, *328*, 360−367.
(24) Zhang, Z.; Ding, Q.; Cui, X.; Jiang, X.; Xing, H. Fine-Tuning and Selective-Binding within an Anion-Functionalized Ultramicroporous Metal-Organic Framework for Efficient Olefin/Paraffin Separation. *ACS Appl. Mater. Inter* **2020**, *12*, 40229−40235.
(25) Zeng, H.; Xie, M.; Wang, T.; Wei, R.; Xie, X.; Zhao, Y.; Lu, W.; Li, D. Orthogonal-array dynamic molecular sieving of propylene/propane mixtures. *Nature* **2021**, *595*, 542.
(26) Hu, P.; Liu, H.; Wang, H.; Zhou, J.; Wang, Y.; Ji, H. Synergic morphology engineering and pore functionality within a metal-organic framework for trace CO_2 capture. *J. Mater. Chem. A* **2022**, *10*, 881−890.
(27) Hu, P.; Wang, H.; Xiong, C.; Liu, H.; Han, J.; Zhou, J.; Zhao, Z.; Wang, Y.; Ji, H. Probing the Node Chemistry of a Metal-Organic Framework to Achieve Ultrahigh Hydrophobicity and Highly Efficient CO_2/CH_4 Separation. *ACS Sustain. Chem. Eng.* **2021**, *9*, 15897−15907.
(28) Wang, Y.; Huang, N.; Zhang, X.; He, H.; Huang, R.; Ye, Z.; Li, Y.; Zhou, D.; Liao, P.; Chen, X.; et al. Selective Aerobic Oxidation of a Metal-Organic Framework Boosts Thermodynamic and Kinetic Propylene/Propane Selectivity. *Angew. Chem. Int. Edit* **2019**, *58*, 7692−7696.
(29) Yoon, J. W.; Kim, A.; Kim, M. J.; Yoon, T.; Kim, J.; Bae, Y. Low-temperature Cu(I) loading on a mesoporous Metal-Organic framework for adsorptive separation of C_3H_6/C_3H_8 mixtures. *Micropor. Mesopor. Mat* **2019**, *279*, 271−277.
(30) Lin, R.; Li, L.; Zhou, H.; Wu, H.; He, C.; Li, S.; Krishna, R.; Li, J.; Zhou, W.; Chen, B. Molecular sieving of ethylene from ethane using a rigid metal-organic framework. *Nat. Mater.* **2018**, *17*, 1128.
(31) Zhang, Z.; Ding, Q.; Cui, X.; Jiang, X.; Xing, H. Fine-Tuning and Selective-Binding within an Anion-Functionalized Ultramicroporous Metal-Organic Framework for Efficient Olefin/Paraffin Separation. *ACS Appl. Mater. Inter* **2020**, *12*, 40229−40235.
(32) Lin, M.; Song, Y.; Lo, P.; Hsu, C.; Lin, A. T. L.; Huang, E. Y.; Chiang, H. K. Quantitative analysis of calcium oxalate hydrate urinary stones using FTIR and 950/912 cm^{-1} peak ratio. *Vib. Spectrosc* **2019**, *102*, 85−90.
(33) Başaran, E.; Demircioğlu, Z.; Tarı, G. Ö.; Ceylan, Ü.; Karaküçük-İyidoğan, A.; Oruç-Emre, E. E.; Aygün, M. Experimental, spectroscopic and theoretical investigation of (+)-(R)-5-[1-(Benzenesulfonamido)-2-phenylethyl]-4-phenethyl-2,4-dihydro-3H-1,2,4-triazole-3-thione. *J. Mol. Struct.* **2022**, *1251*, 131996.
(34) Piña-Beltrán, D. U.; Hernández-Tenorio, C.; Escobedo, C. A. C.; Villanueva-Castañeda, M.; Moreno-Saavedra, H. Electrodeposition and characterization of polypyrrole films on T304 stainless steel. *MRS Advances* **2022**, *7*, 69−72.
(35) Long, R. Q.; Yang, R. T. In Situ FT-IR Study of Rh−Al−MCM-41 Catalyst for the Selective Catalytic Reduction of Nitric Oxide with Propylene in the Presence of Excess Oxygen. *J. Phys. Chem. B* **1999**, *103*, 2232−2238.
(36) Cheng, J.; Zhong, Z.; Lin, Y.; Su, Z.; Zhang, C.; Zhang, X. Miscibility of isotactic poly(1-butene)/isotactic polypropylene blends studied by atomic force Microscopy−Infrared. *Polymer* **2022**, *239*, 124445.
(37) Pavon, C.; Aldas, M.; Rayón, E.; Arrieta, M. P.; López-Martínez, J. Deposition of gum rosin microspheres on polypropylene microfibres used in face masks to enhance their hydrophobic behaviour. *Environmental Technology & Innovation* **2021**, *24*, 101812.
(38) Al-Attas, T. A.; Marei, N. N.; Yong, X.; Yasri, N. G.; Thangadurai, V.; Shimizu, G.; Siahrostami, S.; Kibria, M. G. Ligand-Engineered Metal−Organic Frameworks for Electrochemical Reduction of Carbon Dioxide to Carbon Monoxide. *ACS Catal.* **2021**, *11*, 7350−7357.
(39) Wang, L.; Xiong, G.; Su, J.; Li, P.; Guo, H. In Situ UV Raman Spectroscopic Study on the Reaction Intermediates for Propylene Epoxidation on TS-1. *J. Phys. Chem. C* **2012**, *116*, 9122−9131.
(40) Siberio-Pérez, D. Y.; Wong-Foy, A. G.; Yaghi, O. M.; Matzger, A. J. Raman Spectroscopic Investigation of CH_4 and N_2 Adsorption in Metal−Organic Frameworks. *Chem. Mater.* **2007**, *19*, 3681−3685.
(41) Xie, W.; Hua, F.; Li, L.; Jiang, D.; Feng, C.; Zhao, H. Synthesis, crystal structure, electrochemiluminescence property of a novel cadmium (II) coordination polymer possessing 4-cyanopyrazole. *Inorg. Chem. Commun.* **2019**, *107*, 107489.
(42) Shen, X.; Zhang, T.; Broderick, S.; Rajan, K. Correlative analysis of metal organic framework structures through manifold learning of Hirshfeld surfaces. *MOLECULAR SYSTEMS DESIGN & ENGINEERING* **2018**, *3*, 826−838.
(43) Xie, W.; Hua, F.; Li, L.; Jiang, D.; Feng, C.; Zhao, H. Synthesis, crystal structure, electrochemiluminescence property of a novel cadmium (II) coordination polymer possessing 4-cyanopyrazole. *Inorg. Chem. Commun.* **2019**, *107*, 107489.
(44) Hu, P.; Han, J.; Zhou, J.; Wang, H.; Xiong, C.; Liu, H.; Zhou, X.; Wang, Y.; Ji, H. Customized H-bonding acceptor and aperture chemistry within a metal-organic framework for efficient C_3H_6/C_3H_8 separation. *Chem. Eng. J.* **2021**, *426*, 131302.
(45) Wu, H.; Yuan, Y.; Chen, Y.; Xu, F.; Lv, D.; Wu, Y.; Li, Z.; Xia, Q. Efficient adsorptive separation of propene over propane through a pillar-layer cobalt-based metal-organic framework. *AIChE J.* **2020**, *66*, e16858.
(46) Velasco, E.; Xian, S.; Yu, L.; Wang, H.; Li, J. Large scale synthesis and propylene purification by a high-performance MOF sorbent Y-abtc. *Sep. Purif. Technol.* **2022**, *282*, 120010.

https://doi.org/10.1021/acscentsci.2c00554
ACS Cent. Sci. 2022, 8, 1159−1168

Supporting information

Quasi-Orthogonal Configuration of Propylene within a Scalable Metal-Organic Framework Enables Its Purification from Quinary Propane Dehydrogenation Byproducts

Peng Hu,[†,1] Jialang Hu,[†,1] Hao Liu,[†] Hao Wang,[†] Jie Zhou,[†]
Rajamani Krishna,[*,§] and Hongbing Ji,[*,†]

[†] Fine Chemical Industry Research Institute, School of Chemistry, Sun Yat-Sen University, Guangzhou, 510275, P.R., China.

[§] Van't Hoff Institute for Molecular Sciences, University of Amsterdam, Park 904, 1098 XH Amsterdam (The Netherlands)

[1] These authors contributed equally to this work.

[*]Email: jihb@mail.sysu.edu.cn; r.krishna@contact.uva.nl

Table of Contents

1. Structural characterizations

1.1. Crystal structure analysis and isotherms adsorption

Powder X-ray diffraction (PXRD) experiment was conducted on the Bruker D8 Advance X-ray diffractometer with Cu Ka emission at room temperature. In situ PXRD patterns were collected at 298 K using a capillary tube packed with the sample, which was firstly evacuated, and then filled with C_3H_6 gas. Then, the Reflex refinements process on C_3H_6-loaded PXRD were carefully conducted through the Reflex Module in Materials Studio *2019* program. Given the fact that a larger number of atoms in one unit cell, the ligand molecule and the gas molecule were both treated as rigid motifs during the refinements process, with the molecule orientation and center of mass freely refined. Finally, the satisfactory *R*-factor and R_{wp} values can be yielded through refining the parameters step by step, including lattice parameters, background, thermal factors, occupancies, profiles, etc.

N_2 adsorption–desorption isotherms were measured through the analyzer (ASAP2460, Micromeritics) at 77 K. The samples were initially degassed under reduced pressure for 12 h at 423 K. Single-gas adsorption experiments of various guests were conducted on the Micromeritic ASAP2020 analyzer. During each experiment, about 150 mg of activated **1** powder was placed in the sample cell and dried for 12 h at 373 K.

1.2. Temperature programmed desorption (TPD) experiments

The TPD experiments were carried out on a gas chromatography workstation at different heating rates from 4 to 8 K min^{-1}. For each operation, 0.02 g of activated **1** sample which had adsorbed guest molecules was packed in a stainless-steel column with an inner diameter of 0.35 cm and a packed length of ca. 0.56 cm. Then the stainless tube was placed in a reaction furnace and heated in the high purity N_2 flow at an initial flow rate of 4 sccm. The desorbed molecule was recorded by using the chromatograph with a TCD detector.

1.3. Calculation of desorption activation energy

Desorption activation energy was an important indicator to assess the binding strength between guest molecule and framework. The TPD curves obtained from chromatograph can be well described by the Polanyi-Wigner equation, which is expressed as Equation 1[1]:

$$r_d = -\frac{d\theta_A}{dt} = k_0\theta_A^m \exp(-E_d RT) \quad (1)$$

where r_d is the desorption rate (mol s^{-1}); θ_A is the fractional surface coverage; k_0 is a constant that depends on the desorption kinetics (s^{-1}); m is the order of the desorption process; E_d is the desorption activation energy of adsorbate (kJ mol^{-1}); R is the gas constant [8.314 J $(Kmol)^{-1}$]. Providing that the desorption process follows first-order kinetics (n = 1), the desorption activation energy can be obtained from Equation 2:

$$\ln\left(\frac{\beta_H}{RT_p^2}\right) = -\left(\frac{E_d}{RT_p}\right) - \ln\left(\frac{E_d}{k_0}\right) \quad (2)$$

where β_H is the heating rate (K min^{-1}) and T_p is the peak desorption temperature (K).

2. Spectroscopy tests

2.1. In situ Fourier transform infrared spectroscopy

The in situ Fourier transform infrared (FTIR) tests were recorded using a Tensor II FTIR spectrometer (Bruker) equipped with an in situ diffuse reflectance cell. Adsorbent was pretreated at 373 K for 6 h (flow rate: 20 sccm) to remove the adsorbed gas impurities and then cooled it to room temperature. After the background signal was collected with the flowing He and then was subtracted. Subsequently, **1** was exposed to propylene with a pressure of 1 atm for 36 h to ensure that the adsorption process has reached equilibrium state. All the spectra were recorded over accumulative 256 scans with a resolution of 4 cm^{-1} in the range of 4000~400 cm^{-1} range.

2.2. In situ Raman spectroscopy test

In-situ Raman spectrum was recorded with a RENISHAW-inVia Raman microscope system (USA). Sample was excited with a focused laser beam (λ = 405 nm), 0.5 mW of output power and 75s of acquisition time were used. First, 0.1 g of **1** sample was placed in heating accessories pure argon gas was bubbled over 20 min to ensure an inert atmosphere. As-synthesized **1** was tested at 298 K and C_3H_6-loaded **1** was activated prior to measurement; activation was implemented in a quartz tube at 373 K for 60 min. Finally, **1** was cooled down to 298 K to get the data. The Raman spectra were recorded in the range of 100~4000 cm^{-1}. Data acquisition were carried out by a computer with Renishaw WiRE Raman software version 2.0.

3. Modeling details

3.1. Crystal modeling and optimization analysis

For isostructural **1**, the Crystallographic data in CIF format have been deposited in the Cambridge Crystallographic Data Centre (CCDC) under deposition numbers: 2084733, which can be obtained free of charge via the link https://www.ccdc.cam.ac.uk/structures/ (or from the Cambridge Crystallographic Data Centre, 12 Union Road, Cambridge CB2 1EZ, U.K.). The initial structure was first optimized in the Dmol^3 module, adopting the generalized gradient approximation (GGA) with the Perdew-Burke-Ernzerhof (PBE) functional. The energy, force and displacement convergence criterions were set as 1×10^{-5} Ha, 2×10^{-3} Ha and 3×10^{-4} Å, respectively. To obtain the gas binding energy, an isolated gas molecule placed in a cell unit (with the same cell dimensions as the MOF crystal). The static binding energy (at T = 0 K) could be expressed: $E_B = E$ (MOF) + E (gas) - E (MOF + gas).

3.2. Grand Canonical Monte Carlo (GCMC) calculation

The preferential binding conformation between guests and MOF structure were initially searched through GCMC simulations. Note that host framework and the gas molecule were both rigid in GCMC simulations through using Metropolis method, so that the produced the host-guest binding energies were equal to adsorption enthalpies. For all the GCMC simulations, the frameworks and the gas molecules were described by the universal forcefield (UFF). The Mulliken charges and ESP charges, calculated by PDFT, were employed to the framework atoms and guest atoms, respectively. The loading steps, equilibration steps and the production steps were all set to 2.0×10^5 and the temperature was set at 298 K. The cut-off radius was chosen as 15.0 Å for the Lennard-Jones (LJ) potential and the long-range electrostatic interactions were handled by the Ewald & Group summation method.

3.3. Molecular dynamics (MD) simulations

MD simulations were carried out in the Forcite module in Materials studio program. The output is a collection of snapshots in time of the trajectories of the atoms, which can be used in subsequent analysis. The initial host-guest configurations for the MD simulations were produced by GCMC simulations. The host framework and the gas molecule were both regarded as rigid. The constant-volume and temperature (NVT) ensemble were adopted to simulate the dynamic processes. The charges and force field were the same with that for GCMC simulations. The Nose-Hoover thermostat and Berendsen barostat were employed for temperature and pressure control, respectively. The Verlet method with a time step of 5 fs was used to integrate the particle equations of motion, and atomic trajectories were recorded every 5 ps. Besides, the velocity verlet algorithm was used for integration in the MD simulations, which were used to constrain rigid bonds and to integrate the equations of motion. MD simulations were then run for 30 ns (i.e., 1×10^6 steps with a time step of 2 fs)

after 5 ns of equilibration. The configurations were further stored every 2000 timesteps. The electrostatic interactions and the van der Waals interactions were evaluated by the Ewald summation method.

4. Calculation of separation potential

4.1. Dual Langmuir-Freundlich parameter fits

Dual-Langmuir-Freundlich isotherm model was adopted to fit the single-component loadings at 298 K, as shown in Equation 3 and 4 [2].

$$q = N_1 \frac{ap^b}{1 + ap^b} + N_2 \frac{cp^d}{1 + cp^d} \quad (3)$$

With *T*-dependent parameters *a* and *c*,

$$a = a_0 exp\left(\frac{E_A}{RT}\right); c = c_0 exp\left(\frac{E_B}{RT}\right) \quad (4)$$

Here, *p* is the pressure of the bulk gas at equilibrium with the adsorbed phase (kPa), *q* is the adsorbed amount per mass of adsorbent (mol kg^{-1}), N_1 *and* N_2 is the saturation capacities of site (mol kg^{-1}) of two different binding sites, *a* and *c* (1 kPa^{-1}) is the corresponding adsorption equilibrium constants reflecting the affinity coefficients of sites 1 and 2, and *b* and *d* represent the deviations from an ideal homogeneous surface for site 1 and 2.

4.2. Calculations of ideal adsorbed solution theory

The gas adsorption selectivity at 298 K and 1 bar was calculated using ideal adsorbed solution theory (IAST) on the basis of the single-component adsorption data. The adsorption selectivity for C_3H_6/C_3H_8 separation is defined by Equation 5 [2]:

$$S_{ads} = \frac{q_1 / q_2}{p_1 / p_2} \quad (5)$$

In above equation, the fitting parameters q_1 and q_2 reflected the molar adsorption in the adsorbed phase in equilibrium with the bulk gas phase with partial p_1 and p_2. In this work, dual-site Langmuir-Freundlich (DSLF) model was applied to fit C_3H_6 and C_3H_8 isotherms.

4.3. Calculations of isosteric heat

The isosteric heat (Q_{st}), being the crucial thermodynamic variable in adsorption process, affording serviceable information about the binding affinity between the adsorbate molecules and the adsorbent surfaces at different coverage. For this sake, the coverage-dependent adsorption enthalpy was evaluated from sorption data profiles measured at 273 and 298 K by adopting virial fitting method. In detail, a Virial-type equation mainly contained parameters a_i and b_i, which were independent of temperature. In the equation, a_i and b_i represent the fitting Virial coefficients, m and n stands for the numbers of coefficients needed to precisely the

isotherms, as shown in Equation 6 [3]:

$$\ln P = \ln n + \frac{1}{T}\sum_{i=0}^{l} a_i n^i + \sum_{j=0}^{m} b_j n^j \quad (6)$$

The value of isosteric heat (Q_{st}) could be achieved by virtue of following Clausius-Clapeyron equation, as defined in Equation 7:

$$Q_{st} = -R\left[\frac{\partial \ln p}{\partial(1/T)}\right]_n = -R\sum_{i=0}^{l} a_i n^i \quad (7)$$

5. Transient breakthrough simulations

The performance of industrial fixed bed adsorbers is dictated by a combination of adsorption selectivity and uptake capacity. Transient breakthrough simulations were carried out for C_3H_6/C_3H_8 (30/30/40, v/v/v) and $CH_4/C_2H_4/C_2H_6/C_3H_6/C_3H_8$ (3/5/6/42/44, v/v/v/v/v) mixtures operating at a total pressure of 100 kPa and T = 298 K, using the methodology described in earlier publications [4-8]. For the adsorber of length, L, cross-sectional area, A, voidage of the packed bed, ε, the volume of MOF is $V_{ads} = LA(1-\varepsilon)$ m^3. If ρ is the crystal framework density, the mass of adsorbent in the bed is $m_{ads} = (1-\varepsilon) \times (L \text{ m}) \times (A \text{ m}^2) \times (\rho \text{ kg m}^{-3})$ kg. The breakthrough simulations are presented in terms of the following parameter, as shown in Equation 8:

$$\frac{(Q_0 = \text{ flow rate at inlet mL min}^{-1}) \times (\text{time in minutes})}{(\text{g MOF packed in tube})} = \frac{Q_0 t}{m_{ads}} = \text{mL g}^{-1} \quad (8)$$

The breakthrough simulations demonstrate the potential of producing product gas C_3H_6 of required purity during the interval $\Delta\tau$.

Notation

a	Langmuir-Freundlich constant for species i at adsorption site A, $P_a^{-\nu_{iA}}$
c	Langmuir-Freundlich constant for species i at adsorption site A, $P_a^{-\nu_{iB}}$
E	Energy parameter, J mol^{-1}
Q_{st}	Isosteric heat of adsorption, J mol^{-1}
c_i	molar concentration of species i in gas mixture, mol m^{-3}
c_{i0}	molar concentration of species i in gas mixture at inlet to adsorber, mol m^{-3}
t	Time, s
T	Absolute temperature, K

Greek letters

ε	voidage of packed bed, dimensionless
ν	Freundlich exponent, dimensionless
ρ	crystal framework density, kg m^{-3}

Supporting figures

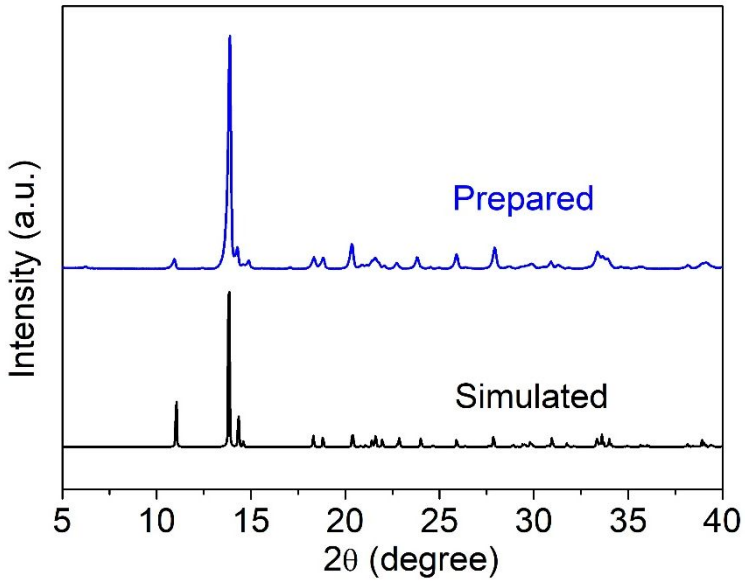

Figure S1. Powder x-ray patterns of **1** simulated from single-crystal topology and obtained experimentally.

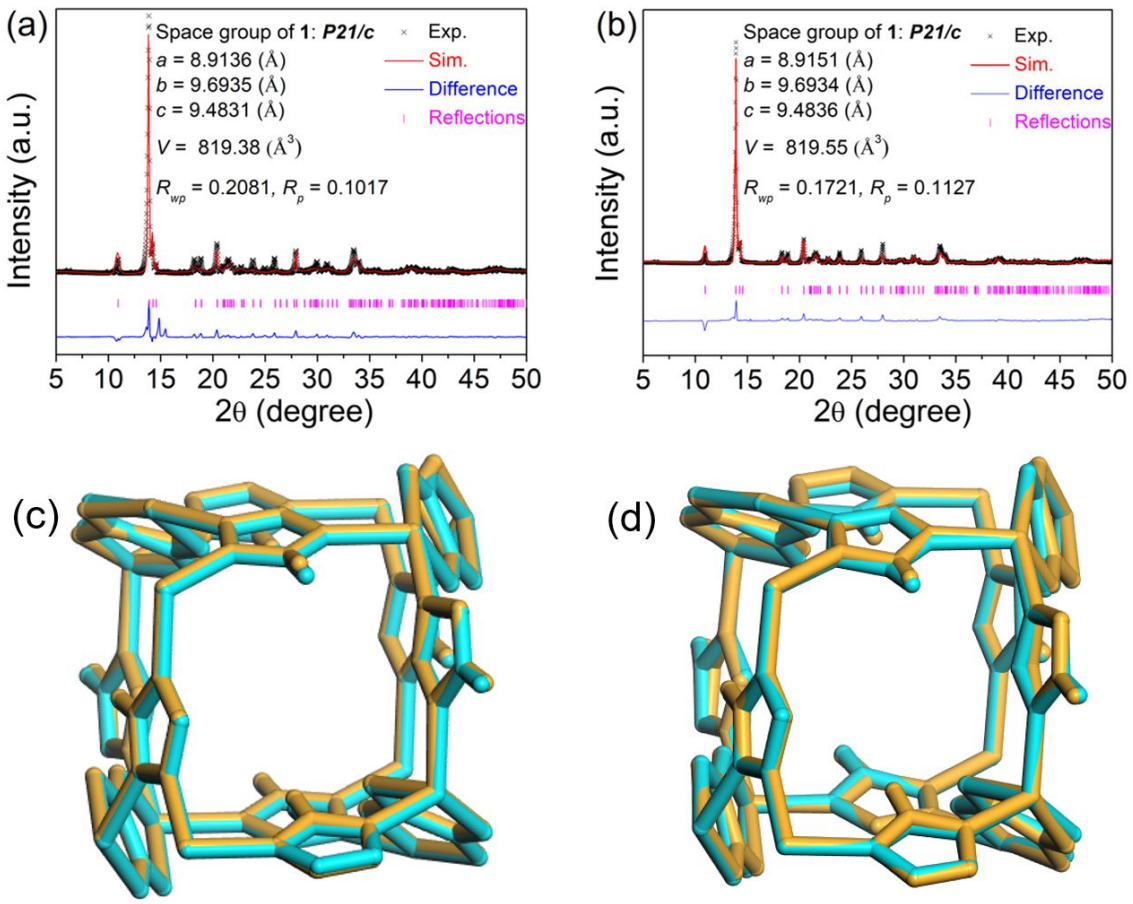

Figure S2. Rietveld structural refinements of **1** recorded at (a) 298 K and (b) 373 K; (c-d) refers to the conformational comparisons of **1** between pristine model structure (orange) and refined structure (turquoise) after heating tests at 298 and 373 K, respectively.

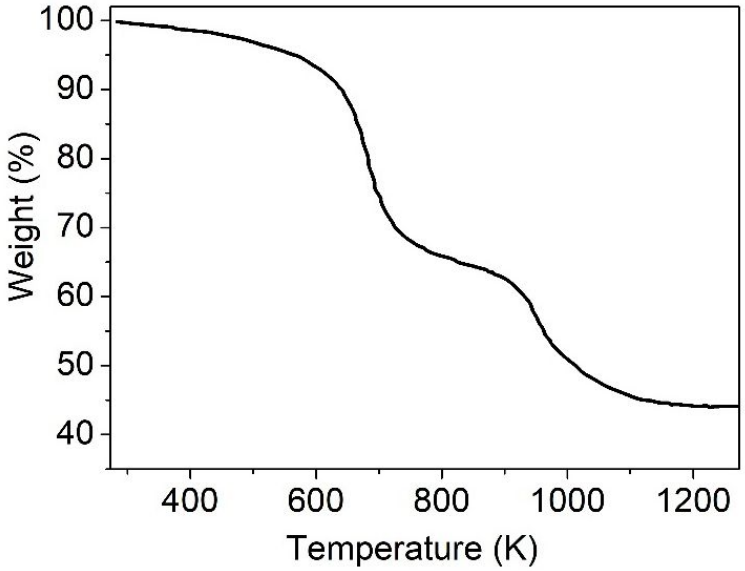

Figure S3. TGA of **1** under air atmosphere.

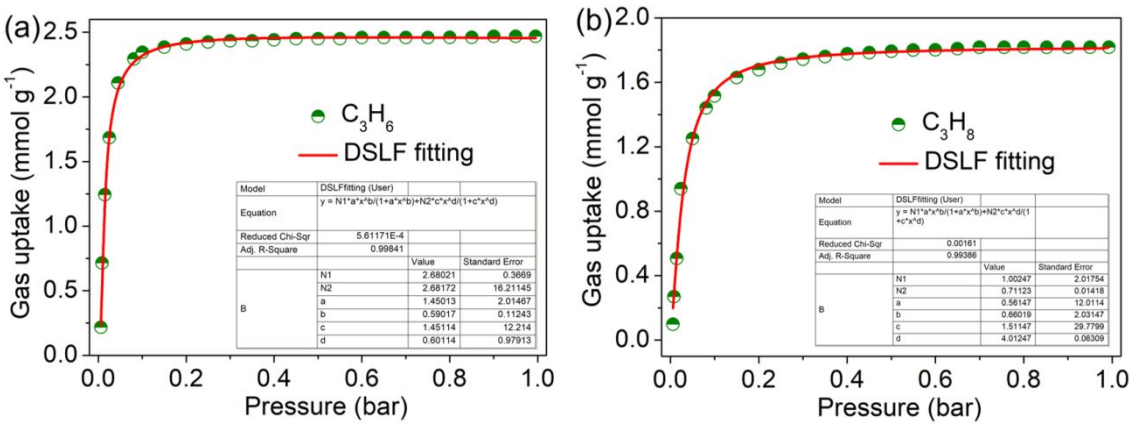

Figure S4. Isotherm fitting of (a) C_3H_6 and (b) C_3H_8 over **1** at 298 K and 1 bar.

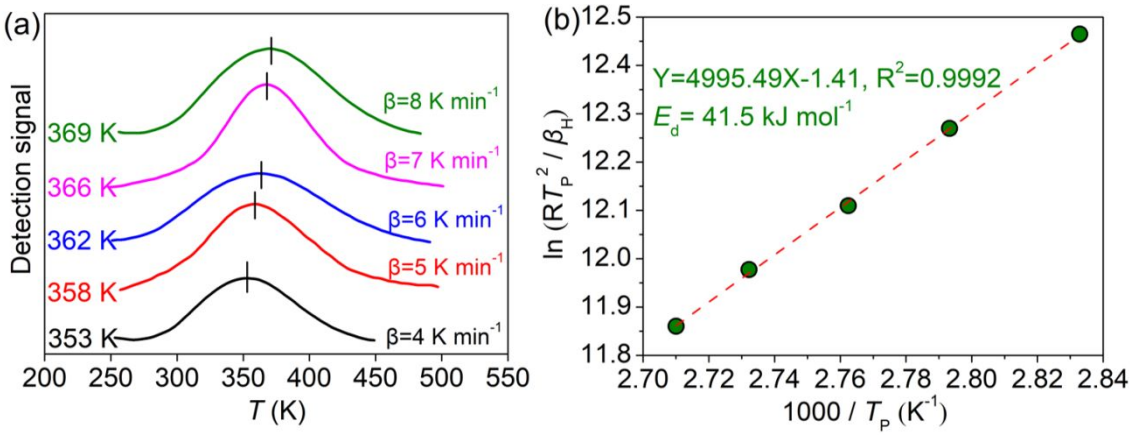

Figure S5. (a) TPD of C_3H_6 on **1** at different heating rates from 4 ~ 8 K min^{-1}; (b) Linear dependence between $-\ln\left(\frac{\beta_H}{RT_p^2}\right)$ and $1000/T_P$ for TPD of C_3H_6 on **1**.

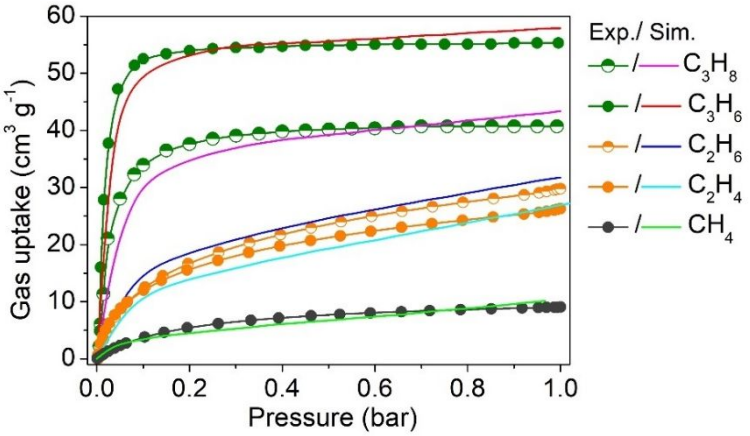

Figure S6. Experimental (dots) and simulated (line) adsorption isotherms of various guests on activated **1** at 298 K and 1 bar.

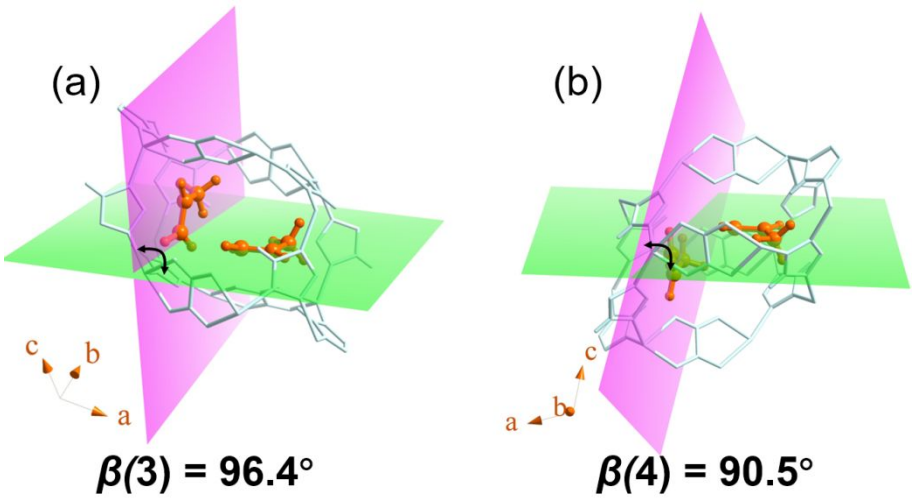

Figure S7. Visualized planes of guest molecule yielded from Figure 3b (**3** and **4**, marking with red color in Figure 3b) and created by three C atoms on a molecule (The atoms in guest molecules are highlighted with orange and other atoms in MOF structure are highlighted with light turquoise for clarity)

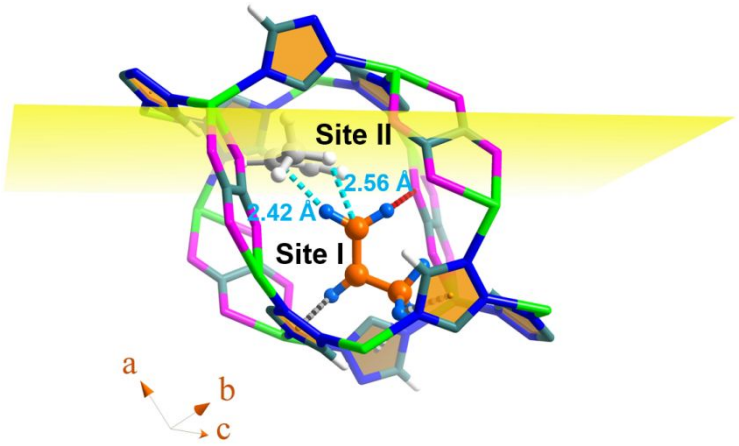

Figure S8. Visualized guest molecule planes created by the three C atoms on a molecule.

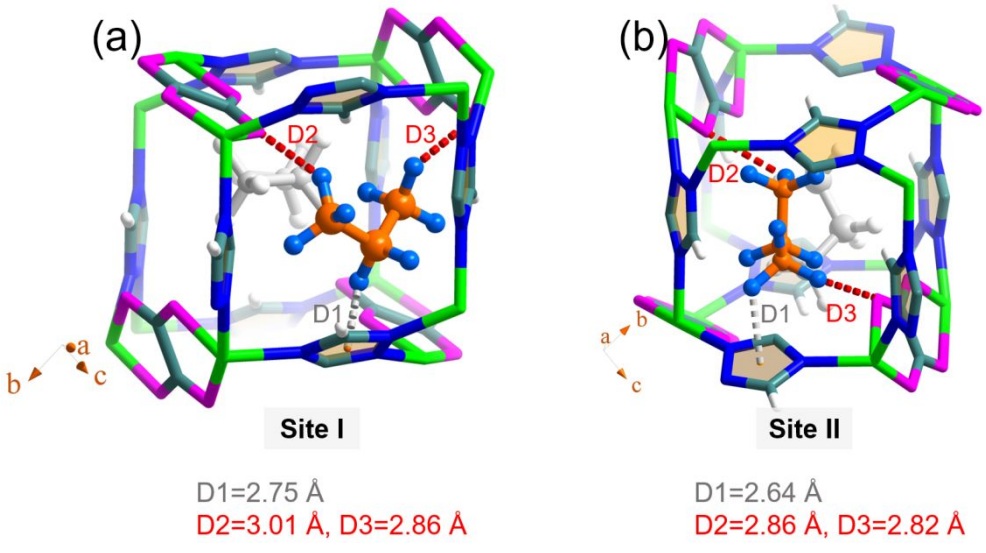

Figure S9. (a) DFT calculated adsorption conformation of C_3H_8-loaded **1** in **Site I** and (b) DFT calculated adsorption conformation of C_3H_8-loaded **1** in **Site II**. (Note that the binding types are colored with gray and red, corresponding to van der Waals interaction and hydrogen-bonding; Color modes: H in ligands, white; H in guest molecule, light blue; Zn, bright green; O, pink; N, blue; C, sea green)

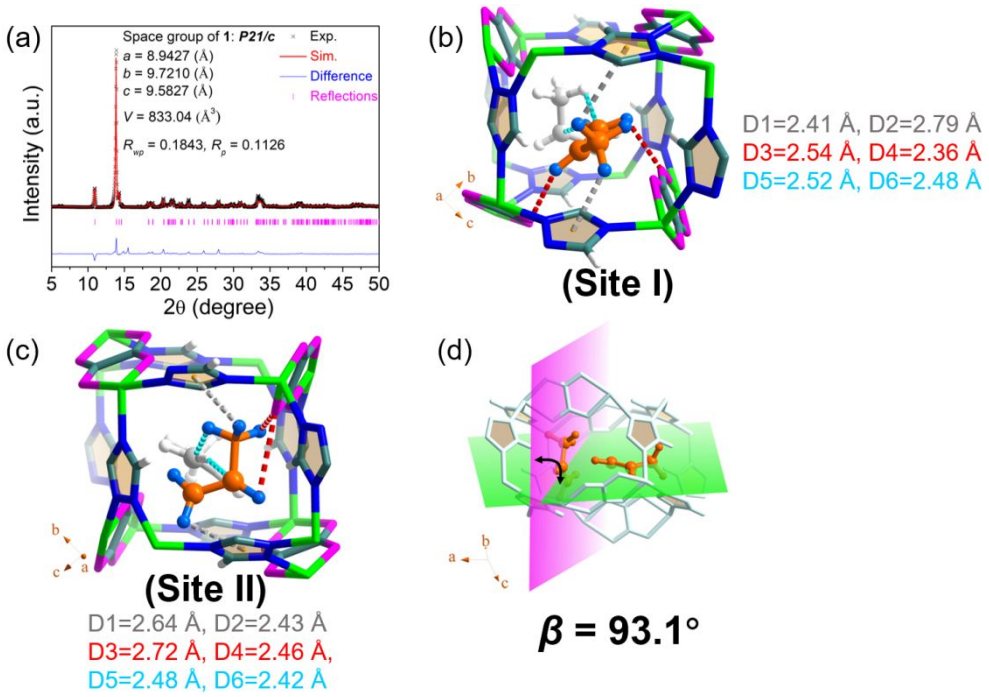

Figure S10. (a) Experimental in situ PXRD pattern (black dots) and refined XRD spectra (red line) of C_3H_6-loaded **1;** Refined geometry conformation of (b) C_3H_6-loaded **1** in **Site I** and (c) C_3H_6-loaded **1** in **Site II**; (d) Visualized guest molecule planes yielded from (b) created by the three C atoms on a molecule.

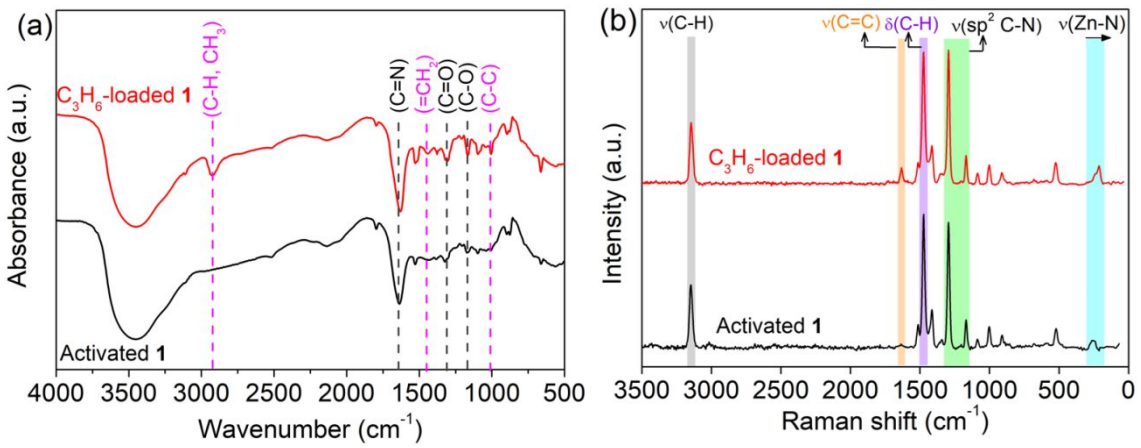

Figure S11. (a) In situ FTIR spectra of activated **1** (black) and C_3H_6-loaded **1** (red) in the wavelength number of 500~4000 cm^{-1}; (b) In situ Raman spectra of activated **1** (black) and C_3H_6-loaded **1** (red), collected with a 405 nm laser.

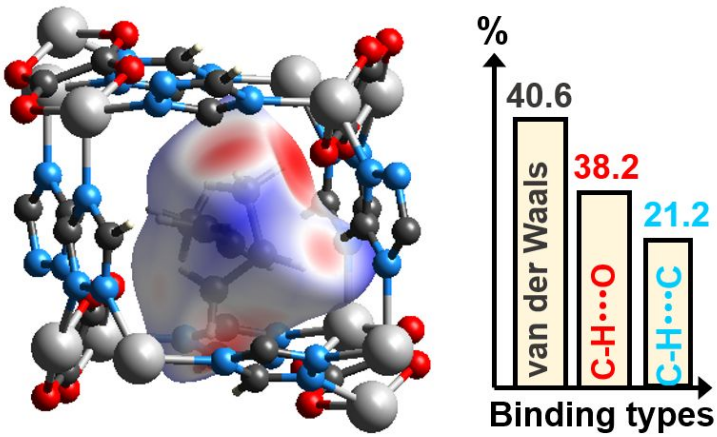

Figure S12. Hirshfeld surface (de) displaying host-guest interactions in **Site II** of C_3H_6-loaded **1** topology.

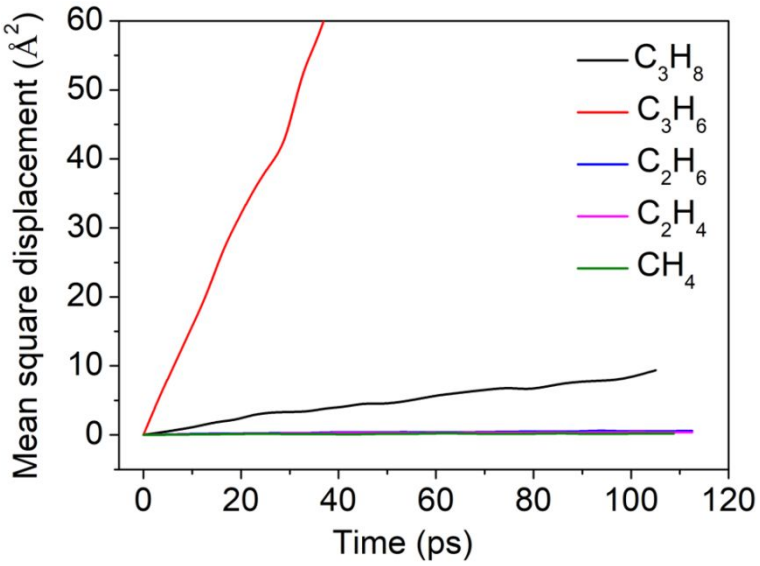

Figure S13. MD-derived self-diffusion rates of various guests in **1**.

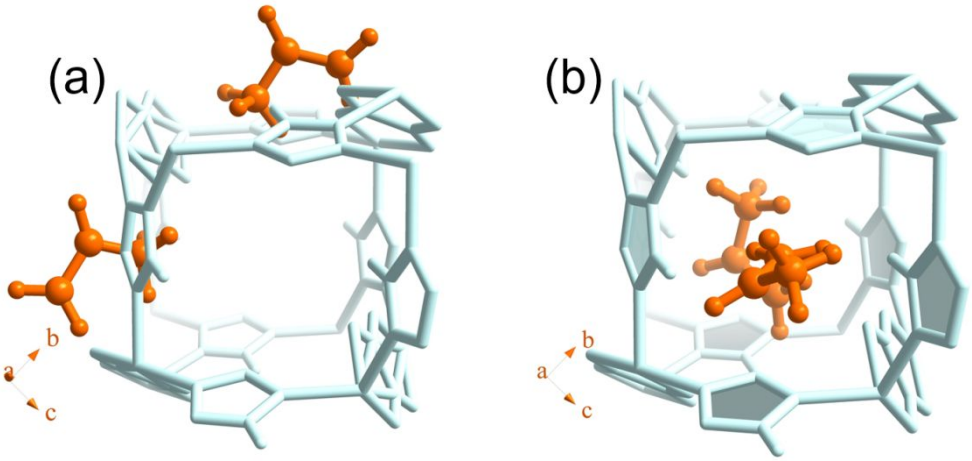

Figure S14. Selected snapshots for MD simulated C_3H_6 adsorption process in **1**: (a) entering aperture of the host framework and (b) staying in the cavity of the host framework with a stable geometry configuration.

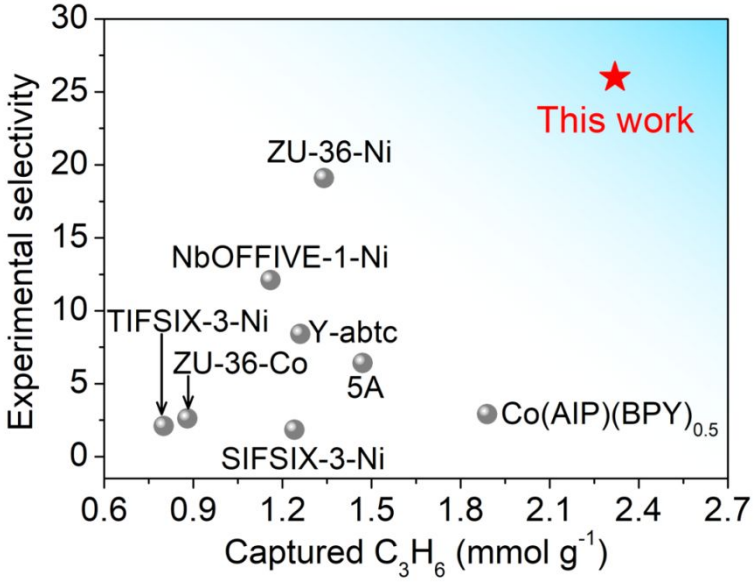

Figure S15. Comparisons of experimental selectivity and C_3H_6 uptake obtained from breakthrough curves over **1** and other benchmark materials.

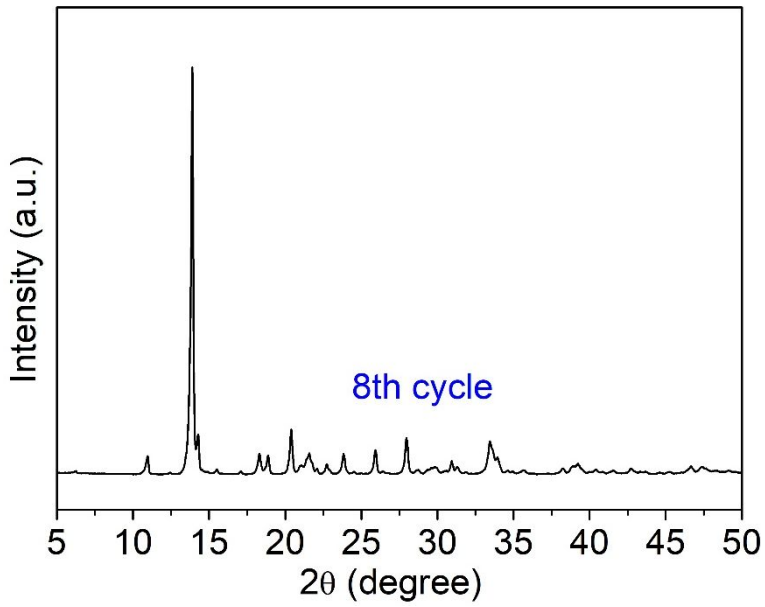

Figure S16. PXRD pattern of **1** after 8th cycle and further immersed in water for one week.

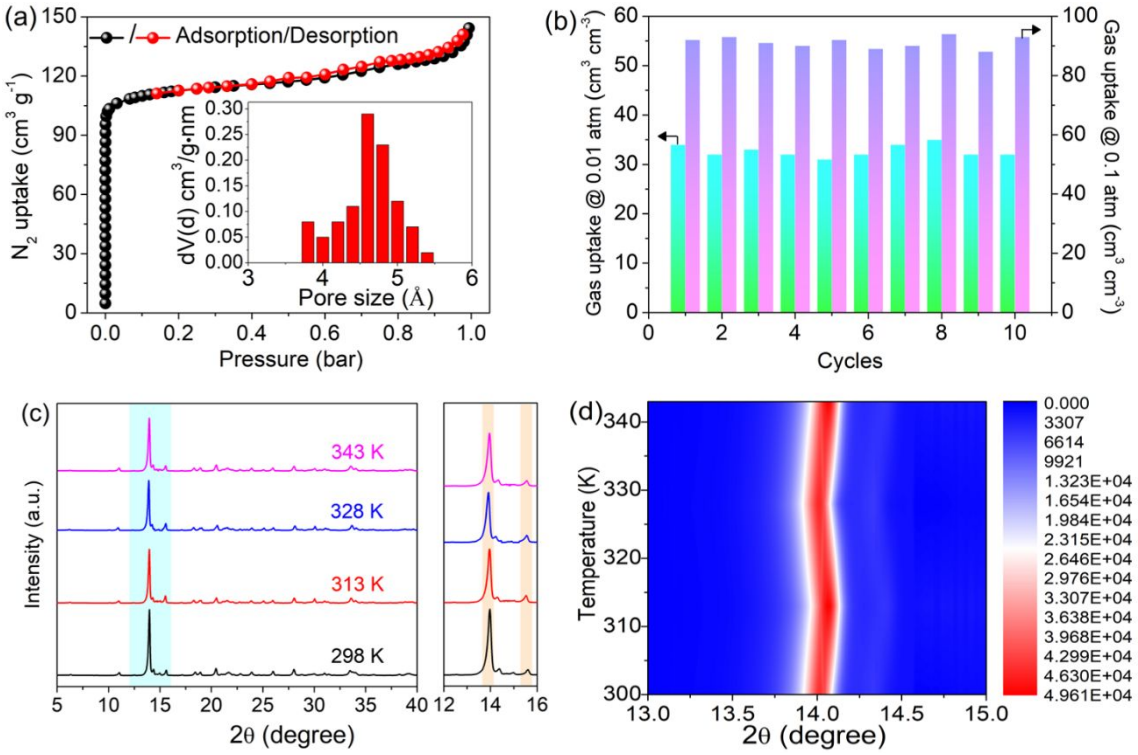

Figure S17. (a) N_2 uptake of **1** after cycling breakthrough tests; (b) Comparison of static C_3H_6 uptake at 0.01/0.1 atm at 298 K after ten cycles; (c) Variable-temperature PXRD of **1** at the temperature of 298 ~ 343 K; (d) Top contour plots of variable-temperature PXRD patters on **1** collected from 298 ~ 343 K in a top view.

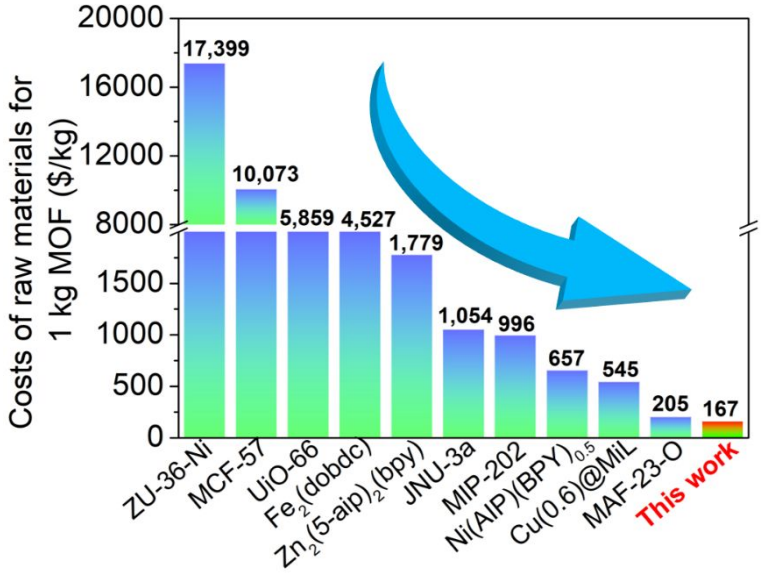

Figure S18. Comparisons of costs of raw materials for **1** and other advanced MOFs.

(For unified comparison, the referenced packages for raw materials and reagents were 100 g and 25 L, respectively)

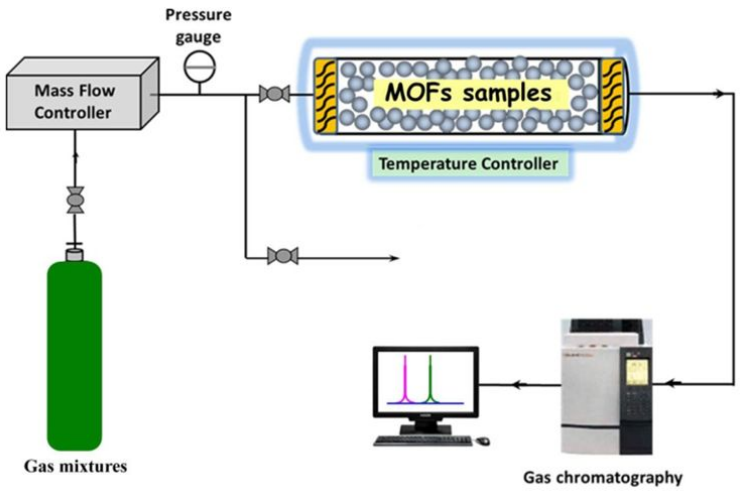

Figure S19. Schematic illustration of the apparatus for the breakthrough tests.

Supporting tables

Table S1. Physical properties of gas molecules used in this work.

Molecule	Kinetic diameter [a] (Å)	Three-dimensional molecule size [b] (Å^3)	Polarizability (× 10^{-25} cm^3)	Dipole moment (× 10^{-18} esu.cm)	Boiling point [c] (K)
CH_4	3.80	3.9 × 4.0 × 4.2	25.93	0	111.5
C_2H_4	4.16	3.4 × 4.2 × 4.9	42.7	0	169.3
C_2H_6	4.44	3.9 × 4.2 × 5.1	44.3-44.7	0	184.4
C_3H_6	4.7	4.16 × 4.65 × 6.45	62.6	0.366	225.5
C_3H_8	5.1	4.20 × 4.80 × 6.80	63.7	0.084	231.0

[a] Kinetic diameter refers to the shortest distance of two colliding identical molecules whose kinetic energies are equal to zero, in which the molecular shape is simplified as a sphere. The value is calculated from the experimental virial coefficients of the gas by assuming that the intermolecular interactions follow the Lenard-Jones potential, but the accurate virial coefficients are very difficult to measure. Therefore, the kinetic diameter of complicated molecules like C_2 differ a lot.

[b] Calculated from the atomic positions from the molecular geometries derived by DFT optimization and corresponding van der Waals radii (C/H/O: 1.7/1.2/1.5 Å).

[c] refers to the value at 298 K.

Table S2. List of atomic positions for Zn-MOF (denoted as **1)** model obtained from crystallography files.

NO.	Element	Symbol	x/a	x/b	x/c
1	Zn	Zn1	0.17588	0.05771	0.43679
2	N	N1	0.0308	-0.1108	0.3683
3	N	N2	-0.0922	-0.1475	0.4100
4	N	N3	-0.0992	-0.2914	0.2259
5	O	O1	0.4098	0.0761	0.6102
6	O	O2	0.6753	0.0307	0.6732
7	C	C1	0.0215	-0.1983	0.2588
8	H	H1	0.0932	-0.1955	0.2086
9	C	C2	-0.1655	-0.2554	0.3232
10	H	H2	-0.2559	-0.3029	0.3289
11	C	C3	0.5248	0.0308	0.5815

Table S3. Crystallographic parameters and refinement details of experimental and theoretical models.

Crystals	**1#**	**1**	**1@298 K**	**1@373 K**
Formula weight	195.72	195.76	195.72	196.75
Crystal system	monoclinic	monoclinic	monoclinic	monoclinic
Space group	***P21/c***	***P21/c***	***P21/c***	***P21/c***
a (Å)	8.9138	8.9139	8.9136	8.9151
b (Å)	9.6934	9.6932	9.6935	9.6934
c (Å)	9.4839	9.4836	9.4831	9.4836
Cell volume (Å^3)	819.46	819.42	819.38	819.55
Calc. density (g cm^{-3})	1.762	1.760	1.762	1.763
R_P (%)	4.17	9.48	10.17	11.27
R_{WP} (%)	10.24	16.11	20.81	17.21

represent the values derived from optimized crystal model.

Table S4. Summary of the adsorption capacity, uptake ratio, selectivities and heat of adsorption data for C_3H_6 and C_3H_8 in various propylene-based MOF adsorbents.

Adsorbents	C_3H_6 uptake [a] ($cm^3\ cm^{-3}$)		IAST [b] (50/50, v/v)		Q_{st} (C_3H_6)[c] ($kJ\ mol^{-1}$)	Ref.
	C_3H_6	C_3H_8	0.1 bar	1 bar		
1	**92.4**	**59.7**	**63.0**	**107.0**	**38.2** [d]	This Work
UiO-66-CF_3	35.2	22.2	82.1	103.0	38.1 [d]	9
MAF-23-O	35.0	18.5	8.9	8.9	54.0 [d]	10
SIFSIX-2-Cu-i	30.5	9.5	4.2	5.1	35.8 [d]	11
Zn_2(5-aip)$_2$(bpy)	36.2	4.0	14.0	20	46.0 [d]	12
CPL-1	5.4	3.8	N.R. [g]	N.R. [g]	N.R. [g]	13
MIL-100(Fe)	40.9	25.8	3.8	2.0	N.R.	14
ZU-36-Co	41.4	8.3	9.5	15	38.0 [d]	15
GeFSIX-2-Cu-i	32.2	13.7	3.8	4.1	36.2 [d]	16
HOF-16a	52.3	33.0	2.0	5.4	30.2 [e]	17
JNU-3a	14.4	7.5	2.7	513	29.3 [f]	18

[a] refers to adsorption uptake at 298 K and 0.1 bar.

[b] IAST selectivity. These values are only for the qualitative comparison purpose.

[c] Q_{st} values at low surface coverage.

[d] refers to Q_{st} was obtained through the virial method.

[e] refers to Q_{st} was obtained through the Clausius-Clapeyron equation.

[f] refers to Q_{st} was obtained through differential scanning calorimetry.

[g] N.R. represent not reported.

Table S5. Dual-site Langmuir-Freundlich parameters fits for C_3H_6 and C_3H_8 of **1**.

		Site A			Site B		
		N_1	a	b	N_2	c	d
		mol kg^{-1}	Pa^{-vA}	dimensionless	mol kg^{-1}	Pa^{-vA}	dimensionless
1	C_3H_6	2.6802	1.4501	0.5902	2.6817	1.4511	0.6011
	C_3H_8	1.0025	0.5615	0.6602	0.7112	1.5115	4.0125

Table S6. The parameters of virial equation for various gas adsorption isotherms on **1**.

Gas	a_0	a_1	a_2	a_3	a_4	a_5	a_6	a_7	b_0	b_1	b_2	R^2
C_3H_8	-3478	401	-882	2001	-1197	2808	-3297	206	18.4	0.017	-0.273	0.9945
C_3H_6	-4608	1468	406	-2808	349	916	-1995	3078	5.78	0.210	-1.27	0.9987
C_2H_6	-2708	822	-1080	2104	204	2747	-3107	76	10.2	-0.004	1.28	0.9889
C_2H_4	-2508	302	-907	1576	198	2574	-2479	128	8.00	0.297	-5.37	0.9967
CH_4	-1008	22	-1026	1508	174	2875	-2439	1022	26.4	0.087	-1.87	0.9937

Table S7. List of atomic positions for C_3H_6-loaded **1** obtained from DFT calculations.

Atom	x/a	x/b	x/c	Atom	x/a	x/b	x/c
O1	0.53007	0.52537	0.2966	O28	0.55843	0.34357	0.55773
O2	0.44157	0.51023	0.2756	C29	0.3405	0.60057	0.4196
C3	0.49173	0.51027	0.30617	H30	0.3644	0.6015	0.40287
Zn4	0.39196	0.48076	0.31226	C31	0.6115	0.58153	0.44107
Zn5	0.60804	0.3141	0.52107	C32	0.50827	0.3436	0.52717
O6	0.53007	0.30797	0.46327	Zn33	0.60804	0.51924	0.3544
O7	0.44157	0.3231	0.44227	N34	0.6564	0.46307	0.37723
C8	0.49173	0.32307	0.47283	N35	0.36407	0.45083	0.36333
N9	0.3026	0.6175	0.47	N36	0.3664	0.40287	0.4247
N10	0.30027	0.56953	0.40863	O37	0.53007	0.52537	0.62993
C11	0.27817	0.58153	0.44107	O38	0.44157	0.51023	0.60893
Zn12	0.27471	0.51924	0.3544	C39	0.6595	0.4339	0.41373
N13	0.32307	0.46307	0.37723	H40	0.6356	0.43483	0.43047
C14	0.32617	0.4339	0.41373	C41	0.3885	0.41487	0.39227
H15	0.30227	0.43483	0.43047	C42	0.49173	0.51027	0.6395
Zn16	0.27471	0.64743	0.52107	Zn43	0.60804	0.64743	0.52107
N17	0.32307	0.37027	0.5439	N44	0.6564	0.37027	0.5439
C18	0.32617	0.39943	0.5804	N45	0.36407	0.3825	0.53
H19	0.30227	0.3985	0.59713	N46	0.3664	0.43047	0.59137
N20	0.3026	0.54917	0.63667	O47	0.53007	0.6413	0.46327
N21	0.30027	0.59713	0.5753	O48	0.44157	0.65643	0.44227
C22	0.27817	0.58513	0.60773	C49	0.6595	0.39943	0.5804
Zn23	0.39196	0.35257	0.47893	H50	0.6356	0.3985	0.59713
N24	0.3436	0.62973	0.4561	C51	0.3885	0.41847	0.55893
N25	0.63593	0.6175	0.47	C52	0.49173	0.6564	0.47283
N26	0.6336	0.56953	0.40863	Zn53	0.39196	0.48076	0.6456
O27	0.46993	0.3587	0.53673	N54	0.3436	0.53693	0.62277
N55	0.63593	0.54917	0.63667	O83	0.55843	0.48977	0.7244
N56	0.6336	0.59713	0.5753	C84	0.50827	0.48973	0.69383
O57	0.46993	0.47463	0.37007	C85	0.38046	0.49996	0.51523
O58	0.55843	0.48977	0.39107	C86	0.4212	0.46972	0.5039
C59	0.3405	0.5661	0.58627	C87	0.4732	0.49803	0.51263
H60	0.3644	0.56517	0.56953	H88	0.3669	0.48094	0.54277
C61	0.6115	0.58513	0.60773	H89	0.34247	0.50784	0.47708

C62	0.50827	0.48973	0.3605	H90	0.40184	0.53348	0.53423
Zn63	0.72529	0.35257	0.47893	H91	0.41015	0.43244	0.49121
N64	0.67693	0.62973	0.4561	H92	0.5013	0.48656	0.49411
C65	0.67383	0.60057	0.4196	H93	0.48358	0.53047	0.5376
H66	0.69773	0.6015	0.40287	C94	0.56762	0.50957	0.46511
N67	0.6974	0.45083	0.36333	C95	0.58889	0.46427	0.49534
N68	0.69973	0.40287	0.4247	C96	0.58856	0.4681	0.54919
C69	0.72183	0.41487	0.39227	H97	0.53398	0.50175	0.42424
N70	0.6974	0.3825	0.53	H98	0.60353	0.5283	0.46206
N71	0.69973	0.43047	0.59137	H99	0.5496	0.53221	0.48667
C72	0.72183	0.41847	0.55893	H100	0.60179	0.43466	0.47675
Zn73	0.72529	0.48076	0.6456	H101	0.61524	0.44389	0.58214
N74	0.67693	0.53693	0.62277	H102	0.56162	0.49515	0.55609
C75	0.67383	0.5661	0.58627				
H76	0.69773	0.56517	0.56953				
Zn77	0.39196	0.6859	0.47893				
O78	0.46993	0.69203	0.53673				
O79	0.55843	0.6769	0.55773				
C80	0.50827	0.67693	0.52717				
Zn81	0.60804	0.51924	0.68774				
O82	0.46993	0.47463	0.7034				

Table S8. Comparisons of binding distances obtained from DFT calculations and in situ PXRD tests.

Binding types	Binding Sites	Distance [a] (Å)	Distance [b] (Å)	Relative error [c] (%)
van der Waals interaction	**Site I**, D1	2.46	2.41	2.0
van der Waals interaction	**Site I**, D2	2.86	2.79	2.4
hydrogen-bonding	**Site I**, D3	2.50	2.54	1.6
hydrogen-bonding	**Site I**, D4	2.37	2.36	0.4
intramolecular interaction	**Site I**, D5	2.56	2.52	1.6
intramolecular interaction	**Site I**, D6	2.42	2.48	2.5
van der Waals interaction	**Site II**, D1	2.59	2.64	1.9
van der Waals interaction	**Site II**, D2	2.48	2.43	2.0
hydrogen-bonding	**Site II**, D3	2.72	2.72	0.0
hydrogen-bonding	**Site II**, D4	2.48	2.46	0.8
intramolecular interaction	**Site II**, D5	2.56	2.48	3.1
intramolecular interaction	**Site II**, D6	2.42	2.42	0.0

[a] represent the binding distance was obtained from DFT calculations

[b] represent the binding distance was obtained from in situ PXRD tests

[c] relative error (absolute value) was calculated based on the equation: $\left[\frac{\text{Distance}^{b} - \text{Distance}^{a}}{\text{Distance}^{a}} \times 100\%\right]$

Table S9. Comparison of simulated diffusion parameters for diffusivity.

Adsorbates	Fitting *K* value ($\times 10^{-3}$)	D_M ($\times 10^{-12}$ m^2 s^{-1})
C_3H_8	80	133
C_3H_6	1550	2580
C_2H_6	4.3	7.17
C_2H_4	3.1	5.17
CH_4	1.3	2.17

Table S10. Estimated raw material cost for the preparation of C_3H_6-selective adsorbents.

Material	Main raw chemicals	Amount of raw(g) per g product	Label[a]	Price ($)[b]	TCPG[c] ($/kg)	Ref.
1	zinc oxalate dihydrate	0.9041 g	Z303988-100 g	8.49	167	This work
	1,2,4-triazole	0.6849 g	T100645-100 g	7.15		
	methanol	9.041 mL	M116115-25 L	102.96		
	ethanol	1.018 mL	E118433-25 L	104.15		
ZU-36-Ni*	nickel tetrafluoroborate hexahydrate	1.199 g	N189039-100 g	65.71	17,399	15
	ammonium hexafluorogermanate	0.7846 g	A167837-5 g	99.68		
	pyrazine	3.523 g	P109613-100 g	26.37		
	water	7.046 mL	W119424-25 L	42.17		
	methanol	7.046 mL	M116115-25 L	102.96		
MAF-23-O	zinc hydroxide	0.3247 g	Z274616-100 g	19.22	205	19
	bis(5-methyl-1H -1,2,4-triazol-3-yl)methane	0.5779 g	A107218-100 g	10.13		
	aqueous ammonia (25%)	12.99 mL	A359072-4 L	19.22		
	water	12.99 mL	W119424-25 L	42.17		
Zn_2(5-aip)$_2$(bpy)	zinc nitrate hexahydrate	1.716 g	Z111703-100 g	25.18	1,880	20
	5-aminoisophthalic acid	0.5228 g	A107450-100 g	16.99		
	4,4'-bipyridine	0.4526 g	B105217-100 g	47.83		
	DMF	117.1 mL	D111999-25L	208.45		
	water	39.02 mL	W119424-25 L	42.17		
UiO-66*	zirconium(IV) chloride	1.207 g	Z109460-100 g	65.41	5,859	9
	terephthalic acid	0.7742 g	P108506-100 g	7.60		
	m-(trifluoromethyl) benzoic acid	0.1055 g	T107270-100 g	22.80		
	DMF	598.1 mL	D111999-25 L	208.45		
JNU-3a	cobalt nitrate hexahydrate	0.7275 g	C112729-100 g	8.34	1,055	18
	5-(3-methyl-5-	0.8100 g	--	---		

	(pyridin-4-yl)-4H-1,2,4-triazol-4-yl)-1,3-benzenedicarboxylic acid					
	methanol	75.00 mL	M116115-25 L	102.96		
	DMA	75.00 mL	D108098-10 L	91.34		
Ni(AIP)(BPY)$_{0.5}$*	nickel acetate tetrahydrate	1.118 g	N112914-100 g	3.13	657	21
	5-aminoisophthalic acid	0.8142 g	A107450-100 g	16.99		
	4,4′-bipyridine	0.3505 g	B105217-100 g	47.83		
	water	44.93 mL	W119424-25 L	42.17		
	methanol	58.41 mL	M116115-25 L	102.96		
MIP-202	zirconium(IV) chloride	1.334 g	Z109460-100 g	65.41	996	22
	L-aspartic acid	1.624 g	A108860-100 g	6.41		
	water	11.60 mL	W119424-25 L	42.17		
MCF-57	cobalt nitrate hexahydrate	0.8595 g	C112729-100 g	8.34	10,073	23
	3-(3-methylpyridin-4-yl)benzoic acid	1.254 g	B176426-100 g	692.55		
	DMA	117.7 mL	D108098-10 L	91.34		
	methanol	58.87 mL	M116115-25 L	102.96		
Cu(0.6)@MIL-100(Fe)*	iron powder	0.2069 g	I116359-100 g	0.92	545	14
	copper(II) chloride	0.3750 g	C106774-100 g	9.54		
	trimethyl 1,3,5-benzenetricarboxylate	0.6259 g	T137552-100 g	73.76		
	nitric acid	0.1490 mL	N116240-500 mL	23.39		
	hydrofluoric acid	0.3222 mL	H278731-2.5 L	12.22		
	water	18.47 mL	W119424-25 L	42.17		
Fe_2(dobdc)	anhydrous ferrous chloride	0.5500 g	I106504-100 g	506.45	4,527	24
	2,5-dioxido-1,4-benzodicarboxylate	0.3050 g	D134233-100 g	136.93		
	DMF	150.0 mL	D111999-25 L	208.45		
	methanol	18.00 mL	M116115-25 L	102.96		

a. The prices are based on Aladdin (https://www.aladdin-e.com/) with the unified package. For unified comparison, the referenced packages for raw materials and reagents were 100 g and 25 L, respectively.

b. Based on average exchange rates as of June 2022, 1 CNY was equal to 0.149 USD.

c. TCPG represent the total costs per gram of adsorbent.

* represent the supposed productivity (80%) of the samples.

References

(1) Sun, X.; Miao, J.; Xiao, J.; Xia, Q.; Zhao, Z. Heterogeneity of Adsorption Sites and Adsorption Kinetics of n-Hexane on Metal−Organic Framework MIL-101(Cr). *Chinese J. Chem. Eng.* **2014**, 22, 962-967.

(2) Hu, P.; Hu, J.; Wang, H.; Liu, H.; Zhou, J.; Liu, Y.; Wang, Y.; Ji, H. One-Step Ethylene Purification by an Ethane-Screening Metal-Organic Framework. *ACS Appl Mater Interfaces* **2022**, 14, 15195-15204.

(3) Hu, P.; Wang, H.; Xiong, C.; Liu, H.; Han, J.; Zhou, J.; Zhao, Z.; Wang, Y.; Ji, H. Probing the Node Chemistry of a Metal-Organic Framework to Achieve Ultrahigh Hydrophobicity and Highly Efficient CO_2/CH_4 Separation. *ACS Sustain. Chem. Eng.* **2021**, 9, 15897-15907.

(4) Krishna, R. The Maxwell−Stefan description of mixture diffusion in nanoporous crystalline materials. *Micropor. Mesopor. Mat.* **2014**, 185, 30-50.

(5) Krishna, R. Methodologies for evaluation of metal−organic frameworks in separation applications. *RSC Adv*. 2015, **5**, 52269-52295.

(6) Krishna, R. Screening metal−organic frameworks for mixture separations in fixed-bed adsorbers using a combined selectivity/capacity metric. *RSC Adv.* **2017**, 7, 35724-35737.

(7) Krishna, R. Methodologies for screening and selection of crystalline microporous materials in mixture separations. *Sep. Purif. Technol.* **2018**, 194, 281-300.

(8) Krishna, R. Metrics for Evaluation and Screening of Metal−Organic Frameworks for Applications in Mixture Separations. *ACS Omega* **2020**, 5, 16987-17004.

(9) Hu, P.; Han, J.; Zhou, J.; Wang, H.; Xiong, C.; Liu, H.; Zhou, X.; Wang, Y.; Ji, H. Customized H-bonding acceptor and aperture chemistry within a metal-organic framework for efficient C_3H_6/C_3H_8 separation. *Chem. Eng. J.* **2021**, 426, 131302.

(10) Wang, Y.; Huang, N. Y.; Zhang, X. W.; He, H.; Huang, R. K.; Ye, Z. M.; Li, Y.; Zhou, D. D.; Liao, P. Q.; Chen, X. M.et al. Selective Aerobic Oxidation of a Metal−Organic Framework Boosts Thermodynamic and Kinetic Propylene/Propane Selectivity. *Angewandte Chemie International Edition* **2019**, 58, 7692-7696.

(11) Wang, X.; Zhang, P.; Zhang, Z.; Yang, L.; Ding, Q.; Cui, X.; Wang, J.; Xing, H. Efficient Separation of Propene and Propane Using Anion-Pillared Metal−Organic Frameworks. *Ind. Eng. Chem. Res.* **2020**, 59, 3531-3537.

(12) Chen, Y.; Wu, H.; Lv, D.; Yuan, N.; Xia, Q.; Li, Z. A pillar-layer metal-organic framework for efficient adsorption separation of propylene over propane. *Sep. Purif. Technol.* **2018**, 204, 75-80.

(13) Chen, Y.; Qiao, Z.; Lv, D.; Duan, C.; Sun, X.; Wu, H.; Shi, R.; Xia, Q.; Li, Z. Efficient adsorptive separation of C3H6 over C3H8 on flexible and thermoresponsive CPL-1. *Chem. Eng. J.* **2017**, 328, 360-367.

(14) Yoon, J. W.; Kim, A.; Kim, M. J.; Yoon, T.; Kim, J.; Bae, Y. Low-temperature Cu(I) loading on a mesoporous Metal−Organic framework for adsorptive separation of C_3H_6/C_3H_8 mixtures. *Micropor. Mesopor. Mat.* **2019**, 279, 271-277.

(15) Zhang, Z.; Ding, Q.; Cui, X.; Jiang, X.; Xing, H. Fine-Tuning and Selective-Binding within an Anion-Functionalized Ultramicroporous Metal−Organic Framework for Efficient Olefin/Paraffin Separation. *ACS Appl. Mater. Inter.* **2020**, 12, 40229-40235.

(16) Wang, X.; Zhang, P.; Zhang, Z.; Yang, L.; Ding, Q.; Cui, X.; Wang, J.; Xing, H. Efficient Separation of Propene and Propane Using Anion-Pillared Metal−Organic Frameworks. *Ind. Eng. Chem. Res.* **2020**, 59, 3531-3537.

(17) Gao, J.; Cai, Y.; Qian, X.; Liu, P.; Wu, H.; Zhou, W.; Liu, D. X.; Li, L.; Lin, R. B.; Chen, B. A Microporous Hydrogen−Bonded Organic Framework for the Efficient Capture and Purification of Propylene. *Angewandte Chemie International Edition* **2021**, 60, 20400-20406.

(18) Zeng, H.; Xie, M.; Wang, T.; Wei, R.; Xie, X.; Zhao, Y.; Lu, W.; Li, D. Orthogonal-array dynamic molecular sieving of propylene/propane mixtures. *Nature* **2021**, 595, 542-548.

(19) Wang, Y.; Huang, N.; Zhang, X.; He, H.; Huang, R.; Ye, Z.; Li, Y.; Zhou, D.; Liao, P.; Chen, X.et al. Selective Aerobic Oxidation of a Metal-Organic Framework Boosts Thermodynamic and Kinetic Propylene/Propane Selectivity. *Angew. Chem. Int. Edit.* **2019**, 58, 7692-7696.

(20) Chen, Y.; Wu, H.; Lv, D.; Yuan, N.; Xia, Q.; Li, Z. A pillar-layer metal-organic framework for efficient adsorption separation of propylene over propane. *Sep. Purif. Technol.* **2018**, 204, 75-80.

(21) Chen, Y.; Wu, H.; Yu, L.; Tu, S.; Wu, Y.; Li, Z.; Xia, Q.Exploiting thermodynamic-kinetic synergetic effect for C_3H_6/C_3H_8 separation in pillar-layer MOFs. *Authorea.* **2021**.

(22) Lv, D.; Xu, J.; Zhou, P.; Tu, S.; Xu, F.; Yan, J.; Xi, H.; Liu, Z.; Yuan, W.; Fu, Q.et al. Highly selective separation of propylene/propane mixture on cost-effectively four-carbon linkers based metal-organic frameworks. *Chinese J. Chem. Eng.* **2022**.

(23) Tian, X.; Zhou, H.; Zhang, X.; Wang, C.; Qiu, Z.; Zhou, D.; Zhang, J. Two Isostructural Flexible Porous Coordination Polymers Showing Contrasting Single-Component and Mixture Adsorption Properties for Propylene/Propane. *Inorg. Chem.* **2020**, 59, 6047-6052.

(24) Geier, S. J.; Mason, J. A.; Bloch, E. D.; Queen, W. L.; Hudson, M. R.; Brown, C. M.; Long, J. R. Selective adsorption of ethylene over ethane and propylene over propane in the metal − organic frameworks M_2(dobdc) (M = Mg, Mn, Fe, Co, Ni, Zn). *Chem. Sci.* **2013**, 4, 2054.